PHOTONICS Research

Advances in on-chip photonic devices based on lithium niobate on insulator

Jintian Lin,[1] Fang Bo,[2,5] Ya Cheng,[1,3,4,6] and Jingjun Xu[2,7]

[1]State Key Laboratory of High Field Laser Physics and CAS Center for Excellence in Ultra-intense Laser Science, Shanghai Institute of Optics and Fine Mechanics (SIOM), Chinese Academy of Sciences (CAS), Shanghai 201800, China
[2]The MOE Key Laboratory of Weak Light Nonlinear Photonics, TEDA Applied Physics Institute and School of Physics, Nankai University, Tianjin 300457, China
[3]XXL—The Extreme Optoelectromechanics Laboratory, School of Physics and Electronic Science, East China Normal University, Shanghai 200241, China
[4]Collaborative Innovation Center of Light Manipulations and Applications, Shandong Normal University, Jinan 250358, China
[5]e-mail: bofang@nankai.edu.cn
[6]e-mail: ycheng@phys.ecnu.edu.cn
[7]e-mail: jjxu@nankai.edu.cn

Received 16 April 2020; revised 24 August 2020; accepted 1 September 2020; posted 2 September 2020 (Doc. ID 395305); published 30 November 2020

Crystalline lithium niobate (LN) is an important optical material because of its broad transmission window that spans from ultraviolet to mid-infrared and its large nonlinear and electro-optic coefficients. Furthermore, the recent development and commercialization of LN-on-insulator (LNOI) technology has opened an avenue for the realization of integrated on-chip photonic devices with unprecedented performances in terms of propagation loss, optical nonlinearity, and electro-optic tunability. This review begins with a brief introduction of the history and current status of LNOI photonics. We then discuss the fabrication techniques of LNOI-based photonic structures and devices. The recent revolution in the LN photonic industry has been sparked and is still being powered by innovations of the nanofabrication technology of LNOI, which enables the production of building block structures, such as optical microresonators and waveguides of unprecedented optical qualities. The following sections present various on-chip LNOI devices categorized into nonlinear photonic and electro-optic tunable devices and photonic-integrated circuits. Some conclusions and future perspectives are provided.

https://doi.org/10.1364/PRJ.395305

1. INTRODUCTION

Information technology driven by the relentless desire for higher capacities of information exchange and processing is reshaping the world. Photons have long been utilized as an information carrier in the communication industry and are now expected to play a central role in information processing. A photonic-integrated circuit (PIC) [1], which is analogous to an electronic integrated circuit, has long been dreamed of, while its functionality is yet to be perfected. The major obstacle toward the realization of an ideal PIC is the downsizing of photonic structures for transmitting and processing light signals in small footprints without degrading the key performances, including propagation loss, tunability, and coupling efficiency [2]. Up to now, silicon-on-insulator (SOI) [3–7], III–V compound semiconductor (InP, GaAs, etc.) [8,9], Si_3N_4 [10–13], Ta_2O_5 [14,15], and polymer [16] have been intensively investigated as candidate platforms for PIC mainly because of ease of formation and low cost when fabricating waveguides based on these materials.

Lithium niobate (LN) has been used to address a considerable number of applications, including data telecommunication as electro-optical modulators, surface acoustic wave devices used in cell phones, and optical frequency conversion for industrial applications and quantum information processing, because of its low absorption loss, wide transparent window (0.35–5 μm), high second-order nonlinear optical coefficient/Pockels electro-optic coefficient, and piezoelectric effect [17–21]. As an element device of the PIC, waveguides on bulk LN are fabricated mostly by metal diffusion, proton exchange, and ion implantation [22]. These waveguides have a relatively large mode field and low refractive-index contrast, leading to large bent radii and impeding its large-scale photonic integration. The recent breakthrough in thin-film LN-on-insulator (LNOI) photonics has provided an unexpected solution due to the excellent optical and electro-optic properties of LN and the planar layered geometry of the LNOI substrate, which is revolutionizing not only the LN industry, but also the modern photonic society [23–27].

The history of thin-film LN technology dates back to 1998 when Levy *et al.* reported on the exfoliation of the first high-quality LN film from a piece of bulk LN crystal by ion slicing [28]. The LN film was sliced from an LN wafer either thermally or chemically by using the change in thermal expansivity or the chemical etching rate of the sacrificial LN layer induced by ion implantation. The LN film thickness can be controlled by tuning the depth of the sacrificial layer in the bulk LN wafer, where the implanted ions gather by adjusting the energy and implant angle of the injected light ions, such as He^+. Most importantly, such an LN film keeps the monocrystalline structure and excellent linear and nonlinear optical properties of the bulk LN crystal after an optimized thermal treatment [29]. The LN film is then polished by chemo-mechanical polishing and bonded onto a support substrate with a transition layer having a low refractive index. Silicon and LN are commonly used as substrates for releasing the thermal expansion mismatch between the LN film and the substrate. Silica, benzocyclobutene, and quartz are used as the transition layer to generate a high refractive index contrast and confine light in the LN film. The thin-film LN is often called LNOI, like the SOI, although silicon is sometimes used as a substrate. A high-quality LNOI substrate was recently commercialized by NANOLN Inc. in China, facilitating dozens of groups in the area of photonics to conduct both fundamental and applied research on the LNOI platform all over the world.

As in SOI, a large index contrast exists between LNOI and air or underneath silica. This characteristic makes it possible to achieve a strong spatial confinement of light within micro/nano-scale photonic structures, which is not only indispensable for achieving high-density PICs and efficient nonlinear optical processes, but also beneficial for low-power-consumption surface acoustic waves, high-speed on-chip modulators, etc. The past decade has seen phenomenal progress in the nanofabrication of LNOI photonic structures. In pioneering works, Guarino *et al.* demonstrated a ring microresonator with a Q factor of only 4.0×10^3 in 2007 [30], while Hu *et al.* demonstrated an optical ridge waveguide with an optical loss of 6.3 dB/cm in 2012 [24]. Today, the highest Q factor of an LNOI microdisk resonator has reached 4.7×10^7 [31], and the lowest optical losses in single- and multimode LNOI waveguides are 0.029 dB/cm [32] and 0.027 dB/cm [33,34], respectively. In other words, the Q factor and optical loss in LNOI photonic structures have improved by four and three orders of magnitude, respectively. The development of LNOI nanofabrication technology has opened the avenue to a wide variety of high-performance and highly functional photonic microdevices, including high-Q whispering-gallery-mode (WGM) resonators [30,35–40], photonic crystal (PhC) cavities [41–43], high-speed electro-optic modulators beyond 100 Gbit/s on pure LNOI [44,45] and hybrid LNOI [45–47] platforms, compact acoustic-optical devices [48–50], highly efficient classical and quantum nonlinear light sources [51–56], frequency microcombs [57–62], on-chip spectroscopy [63,64], high-dimension communication [65], etc. Novel LNOI photonic structures and devices have attracted significant interest from researchers in the fields of nanophotonics, nonlinear optics, optical communication, quantum information processing, and microwave photonics, to name a few [23–26,30,35,37–40,44,66–73].

At present, LNOI photonics is still in its infant stage. On one hand, the development and refinement of fabrication techniques do not seem to cease, as driven by the desire for an even higher optical performance. On the other hand, novel devices of unique functionalities have continuously been conceived and designed, and some of them have already been experimentally demonstrated. Many of the latest achievements could not have been foreseen, even a few years ago, which, however, indicate enormous opportunities for the future development of this area, as to be identified in this review [23–27,74,75]. Note that several highly influential review papers covered LNOI photonics [23,24,26,27,75], ranging from the fabrication of LNOI and basic photonic devices to electro-optic modulators and nonlinear optical applications. The manufacturing methods for fabricating LNOI photonic devices promoting the rapid development of LNOI photonics, which are distributed in many original papers, must be summarized. This review will focus on photonic device manufacturing and the new development of LNOI photonics. We will describe and compare the fabrication techniques and domain polarization methods (Sections 2 and 3) and discuss the development and application of LNOI devices in PICs, such as electro-optic modulation and acoustic optics (Section 4.A), nonlinear optics (Section 4.B), and other PICs (Section 4.C). Lastly, we will summarize the aforementioned milestone results and give a future outlook of this vibrant and promising field of research.

2. CUTTING-EDGE LNOI FABRICATION TECHNOLOGIES

A. Early Attempts on Fabricating LNOI Photonic Microstructures

Both high- and low-index-contrast waveguides can be produced in an LNOI. Low-index-contrast waveguides are used in constructing photonic microdevices, such as beam deflector-based switches [76], modulators [77], and electric field sensors [78]. Meanwhile, weak optical guiding and poor optical confinement give rise to a large radius of the bending curvature (mm/cm scale) and low density of photonic integration. This problem can be solved by developing a nanofabrication technology of high-index-contrast LNOI photonics, which requires wet or dry etching of the LNOI. The wet etching of bulk LN by hydrofluoric acid (HF) or potassium hydroxide (KOH) has a long history and inherently suffers from high surface roughness, low etching rate, and an unfavorable sensitivity to the crystallographic orientation, which results in poor electro-optic and nonlinear optical applications. The etching rates of LN with HF solution have a unisotropic feature as a consequence of the uniaxial crystal structure of LN relying on the material's ferroelectric properties. The etching rate of the $-Z$ face (i.e., the negative electric surface perpendicular to the c axis) of LN is appreciably higher than that of the $+Z$ face with HF acid. Fabricating LN microdevices by wet etching generally starts from the $-Z$ face. Differential etching via domain inversion can be used to fabricate LN microstructures [79]. Some treatment techniques, such as proton exchange, ion diffusion, and ion implantation, have been used to preprocess LN prior to wet

etching to improve the HF etching rate and/or selectivity for a given surface of the LN crystal [80–87]. Ion implantation is used to modify LN crystals based on two effects: (1) change of refractive index and (2) lattice damage [88]. An optical waveguide fabricated on an LNOI by Ar ion implantation and subsequent wet etching (KOH) shows an optical loss of 61 dB/cm at 1.411 μm wavelength [89]. Today, instead of being used in fabrication, wet etching is more frequently used to reveal the domain and defect structures in LN crystal.

Compared with wet etching, dry etching is often more controllable and has the advantage of high anisotropy. Ion beam milling has been applied to bulk LN since the mid-1970s [90,91]. Photonic devices on LNOI can also be fabricated by relying on dry etching at room temperature involving processes such as reactive ion etching (RIE) based on fluorine (sometimes chlorine) gases produced by the discharge [81,92–100], Ar ion milling [30,37,38], focused ion beam (FIB) milling [24,35,39], and photolithography-assisted chemo-mechanical etching (PLACE) [31–33,101–103]. Here, RIE and Ar ion milling are complementary metal oxide semiconductor (CMOS)-compatible nanofabrication techniques. However, RIE often results in high scattering loss because of the formation and redeposition of non-volatile LiF on the surface during the etching process. Another alternative solution for reducing the LiF redeposition is adding Ar gas in fluorine gases to physically bombard the target and enhance the sputtering process during etching [92,94,99] and using pure Ar gas without fluorine gases to avoid the LiF redeposition [30,98]. The control of the edge and surface roughness in photoresist patterns has been recognized as critically important in fabricating LNOI nanostructures with lithography and Ar ion milling, as we will discuss in Section 2.B.

Photolithographic structuring with Ar ion milling has been performed to fabricate photonic devices on the LNOI, such as ridge waveguides [98] and microring resonators [30], since 2005 and 2007, respectively. Figures 1(a) and 1(b) show the fabricated microring. The limited Q factor was caused mainly by the roughness (~4 nm) of the top surface and the sidewall, as evidenced by the scanning electron microscope (SEM) image in Fig. 1(b). The root mean square (RMS) surface roughness of the sidewall and the surface of the fabricated LN ring by Ar ion milling was 4 nm; thus, a SiO_2 layer was used to cover the LN thin film to reduce the scattering loss of the microdevice. The loaded Q factor was measured as 4.0×10^3 around the 1550 nm wavelength and corresponded to a propagation loss of 4 dB/cm of the ridge waveguide.

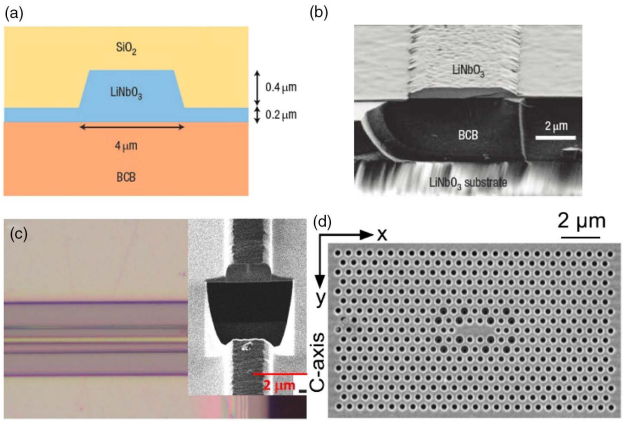

Fig. 1. (a) LNOI microring fabricated by Ar ion milling [30]. (b) Scanning electron microscope (SEM) image of the cross section of the ridge waveguide showing relatively rough surface and sidewall. (c) Optical microscope image of a ridge waveguide fabricated by FIB [24]. Inset: SEM image of the cross section of the ridge waveguide showing a rough surface. (d) SEM image of the PhC microcavity fabricated by FIB [104].

Other than Ar ion milling, nano-scale photonic devices were also fabricated using FIB in 2009 [43]. FIB is a physical etching process that is also based on ion bombardment. Due to the small focal spot size of an ion beam, FIB is of an extremely high fabrication resolution and can produce surfaces of low roughness [105,106]. The ridge waveguide was demonstrated on the LNOI [24] [Fig. 1(c)], indicating a surface smoother than that shown by Ref. [30] obtained with Ar ion milling. However, the top surface showed a significant roughness due to the redeposition. In another experiment reported in 2013, a PhC L3 cavity fabricated on the LN membrane by FIB milling with a helium ion showed a Q factor of 535 [104] [Fig. 1(d)]. The main restriction of FIB when fabricating LNOI photonic structures and devices is its low fabrication efficiency. In promoting fabrication efficiency, the rough milling mode is typically chosen to enhance the sputtering rate while redeposition becomes more severe at a higher sputtering rate, becoming responsible for a higher surface roughness. As an expensive and time-consuming process [105–107], FIB is unsuitable for fabrication of large-scale photonic structures.

The abovementioned pioneering works demonstrated the feasibility of fabricating nanophotonic structures on the LNOI and revealed the difficulties in reducing propagation loss by suppressing the surface roughness [108]. The key to obtaining a smooth edge and surface of the photoresist patterns in Ar ion milling is to choose suitable lithographic techniques. In FIB, the key is to enable fine milling to reduce the redeposition while maintaining sufficient fabrication efficiency for photonic structures of relatively large area sizes. The most important message from the pioneering works is that the major source of the inferior optical quality of LNOI photonic structures fabricated by ionic dry etching is the surface roughness, not the intrinsic absorption of the LNOI material. The breakthroughs in LNOI nanophotonics over the past five years benefited mainly from the technical innovations and refinements that gradually brought down the surface roughness of LNOI nanostructures from tens of nanometers to below 1 nm.

B. Fabrication Techniques of Low-Loss LNOI Nanophotonic Structures

In 2014, Lin *et al.* first showed that high-Q microresonators with a Q factor above 10^5 could be readily achieved if the surface roughness of the LNOI nanostructures could be sufficiently suppressed [35,39]. The Q factor was soon promoted to be above 10^6 by refining the fabrication parameters [40,51]. The technique is still based on FIB, but the FIB milling process is conducted twice, with the second process performed at a low current and low writing speed to achieve surface smoothness as high as possible. Conventionally, this strategy is impractical because of the unacceptable time consumption of FIB milling

under such a fine milling operation mode. However, the group successfully reduced the total time of the fabrication process by first creating a semifinished microdisk by femtosecond laser micromachining [35,39]. Due to the relatively high scanning speed and micrometer-scale fabrication resolution of femtosecond laser micromachining, the semifinished microdisk can typically be fabricated in less than 1 h. Subsequent FIB milling is required only to smoothen the microdisk sidewall, but not for material removal, which can be done in several or tens of minutes for a microdisk.

Figure 2(a) shows the process flow of the fabrication of the high-Q microresonator. First, a microcylinder was produced on the LNOI via water-assisted femtosecond laser ablation. The surface was kept intact with an RMS roughness of 0.5 nm [23]. The sidewall formed by laser ablation was rough on the order of several tens of nanometers and not smooth enough for photonic applications. Second, two-step FIB milling was performed to polish the sidewall to reduce the scattering loss, beginning with coarse milling, followed by fine milling, to eliminate the redeposited LN induced by coarse milling. A smooth sidewall was obtained after FIB polishing. Third, the silica layer underneath the LN thin-film disk was selectively removed into a small pillar by HF wet etching. Last, the partially free-standing microdisk ensured annealing at 500°C to reduce the scattering loss by partial recovery of the lattice damage induced by ion scattering. A higher temperature will cause the device to break due to the thermal expansion mismatch between the LN film and silica transition layer. Figure 2(b) depicts a typical microdisk resonator with a smooth sidewall and surface. In 2014, the loaded Q factor of the fabricated LNOI microdisk was 2.5×10^5 around 1550 nm wavelength, which was soon improved to 2.45×10^6 in 2015.

The work by Lin *et al.* clearly showed the critical importance of suppressing the surface roughness when fabricating high-Q LNOI nanophotonic structures [110]. Once the philosophy was established, progresses were made with other lithographic fabrication techniques. In 2014, Wang *et al.* achieved an LNOI microdisk with a Q factor higher than 10^5 using electron-beam lithography (EBL) for patterning a photoresist, followed by subsequent Ar ion milling [38]. The fabrication resolution of EBL is much higher than that of optical or laser lithography, leading to significant improvement in the edge roughness of photoresist patterns. On the contrary, although EBL is a slow process, it is much faster than FIB, thereby allowing the production of a variety of novel nanophotonic devices on the LNOI in many research laboratories worldwide, due to the popularity of the EBL and RIE systems [44,60,71,111–117]. Ar ion milling is typically performed in RIE and inductive coupled plasma (ICP)–RIE systems. The ICP tool is used to generate high-density plasma for deep etching. The neutral loop discharge (NLD) is another approach for generating high-density plasma at a low RF bias voltage. The NLD plasma is used to fabricate a ridge LN waveguide with a slope angle of more than 70° [118]. However, the sidewall smoothness is relatively high [118–121].

Another lithographic technique for generating the photoresist patterns of low edge roughness is ultraviolet (UV) lithography, which was first demonstrated by Wang *et al.* [37]. Figure 3(a) schematically illustrates the process flow of fabrication. A disk-shaped photoresist pad was produced by spin-coating, followed by transferring the pattern from a photomask using UV lithography [37,122,123]. This photoresist pad then served as an Ar ion etching mask, and the exposed LN thin film ensured Ar ion etching. The etching selectivity between the photoresist mask and LN was 4:1, which can be improved using a chromium (Cr) mask [124]. A partially free-standing LN microdisk was obtained after the removal of the residuary photoresist and the HF under-etching of silica [Fig. 3(b)]. The loaded Q factor of the fabricated microdisk was a record high value at that time, reaching above 10^6.

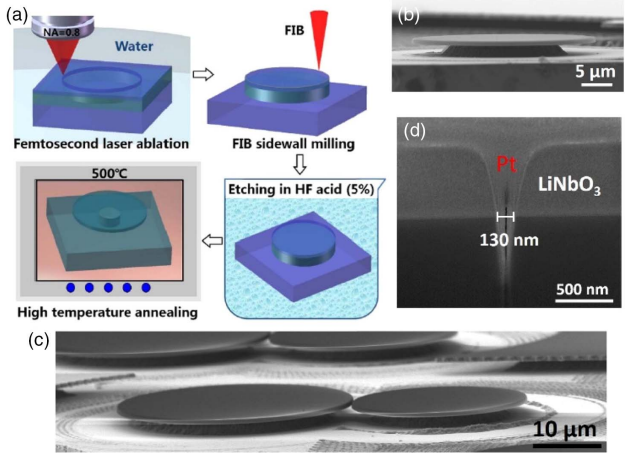

Fig. 2. Microresonators fabricated by femtosecond laser ablation and FIB polishing: (a) schematic illustration of the process flow of the fabrication [35,39]; (b) SEM image of a single microdisk with Q of 9.61×10^6 [51] showing smooth sidewall and surface; (c) SEM image of a coupled double-microdisk with 123 nm gap [109]; and (d) enlarged SEM image of the coupled region coated with platinum (Pt) for imaging.

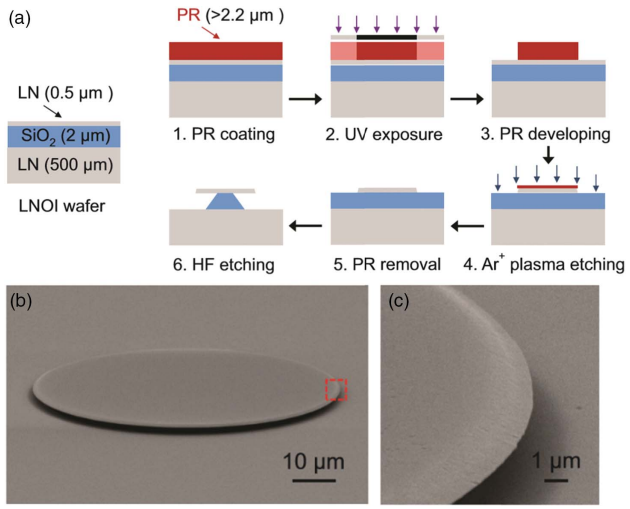

Fig. 3. Microresonator fabricated by UV lithography and Ar ion milling [37]: (a) schematic illustration of the process flow of fabrication; and (b), (c) SEM images of the microdisk showing smooth sidewall and surface.

The abovementioned techniques have their own strengths and weaknesses. The EBL, followed by Ar ion milling, can provide a reasonable fabrication efficiency and a sub-micrometer resolution, while UV lithography, followed by Ar ion milling, is more advantageous for the mass production of LNOI micro- and nanostructures, but with a limited fabrication resolution due to the optical diffraction limit. When preparing samples of low quantities, UV lithography is also not as flexible as EBL because the latter requires a projection mask. Meanwhile, femtosecond laser machining, followed by FIB milling, can provide the highest fabrication resolution and reasonable fabrication efficiency [51]. This technique requires unconventional equipment and technical expertise, which are not easily accessible.

C. Fabrication Techniques of Ultralow-Loss LNOI Nanophotonic Structures

A congruent LN crystal has a very low intrinsic absorption of light (e.g., its absorption coefficient is $\alpha \leq 4 \times 10^{-4}\,\mathrm{cm}^{-1}$ at 1310 nm wavelength, which corresponds to an intrinsic $Q \approx 2 \times 10^8$) [108]. The loaded Q factors shown in Section 2.B were approximately two orders of magnitude lower than the theoretical limit of the intrinsic Q factor of a congruent LN. The comparison suggests that the loss results mainly from the scattering by the residual roughness at the sidewall of the ion-etched photonic devices, which is typically on a nanometer level.

In general, two approaches can be used to reduce scattering losses at the rough surfaces of the LNOI nanostructures: one is to reduce the roughness itself, and the other is to reduce the refractive index contrast between LN and its surrounding environment [30]. The first approach is more challenging, but will ultimately solve the problem without influencing the characteristics of the fabricated photonic structures. The second approach can be more easily implemented. In 2017, it was investigated by Zhang *et al.* [34], and they showed that by covering a super-smooth microring fabricated by EBL patterning and Ar ion milling with a SiO_2 layer, the loaded Q factor of the microring can be improved to 5×10^6, which corresponded to an intrinsic Q factor of 1.0×10^7. This value is almost one order of magnitude higher than that of similar devices without the SiO_2 coating. They also showed a propagation loss of 0.027 dB/cm in the straight multimode ridge waveguide [34].

Chemo-mechanical polishing (CMP) was employed to polish the sidewall of the formed microstructures to promote the sidewall smoothness and to ultimately eliminate the source of scattering loss [100]. CMP is a traditional fabrication technique frequently used in the semiconductor industry to fine polish the wafer surface and in the photonics industry to form bulk optical devices. It is also used in LNOI wafer fabrication to remove the ion damage surface layer of the ion-sliced LNOI thin film with 0.5 nm roughness [23]. A microring covered with a Cr hard mask was fabricated by UV lithography, followed by RIE [Fig. 4(a)]. The sidewall of the microring was initially quite rough, as shown in Fig. 4(c). Thus, CMP was introduced to polish the sidewall. Cr was used as the etching/polishing mask because of its high hardness (Mohs hardness: 8). The microstructure sidewall was in contact with the polishing slurry dispersed in a soft polishing pad. Therefore, this sidewall

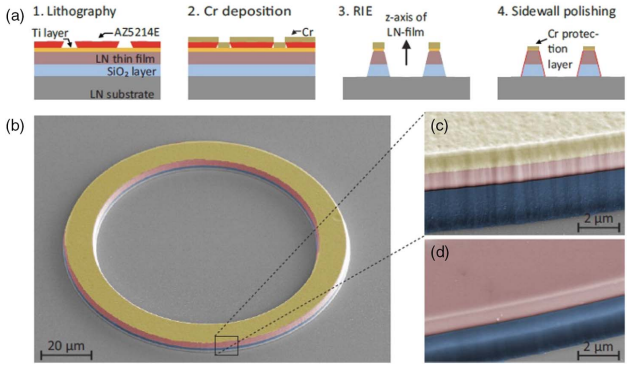

Fig. 4. Microring fabricated by UV lithography and RIE, followed by sidewall polishing by the CMP [100]: (a) schematic illustration of the process flow of fabrication; (b) false-color SEM image of the microring; and enlarged SEM image of the sidewall (c) before and (d) after the CMP.

was contacted and polished, while the top surface underneath the hard mask was kept intact. The sidewall roughness was reduced to 4 nm. Figure 4(d) shows the microring of the Q factor $>3 \times 10^6$ [100] (the highest Q was 9×10^6 in Ref. [125]) fabricated by RIE and CMP. The ridge waveguide of the propagation loss <0.04 dB/cm can be obtained by this technique [125].

The typical difficulty in completely eliminating the surface roughness left behind by Ar ion milling with the additional CMP process is that the CMP cannot achieve the same level of surface roughness on the steep sidewall as that on a flat horizontal surface. In addition, the ionic dry etching often induces inner lattice damage in the LN thin film. Luckily, the CMP alone can be used as an efficient means for pattern transfer in lithographic fabrication [103]. Figures 5(a)–5(e) schematically illustrate the process flow of the fabrication technique, PLACE. First, a Cr mask deposited on LNOI was patterned on the LNOI by femtosecond laser direct writing. The Cr film is of a higher hardness than that of the LN film; thus, the pattern was transferred from the Cr mask to the LN thin film via etching of the exposed LN film using the CMP process. Finally, the Cr mask was removed by chemical wet etching. Figure 5(e) depicts the experimental setup for the CMP, where the soft velvet cloth used in CMP allows not only the Cr film, but also the exposed LN film to be in contact with the polishing slurry. Ultra-loss ridge waveguides with a propagation loss of 0.027 dB/cm and an ultrahigh loaded Q factor of 4.7×10^7 microdisk were demonstrated around 1550 nm wavelength [31,33] [Figs. 5(f)–5(i)]. In addition, single-mode ridge waveguides with a propagation loss of 0.029 dB/cm were demonstrated by adding a Ta_2O_5 cladding layer on the LNOI waveguides [32,126]. The RMS roughness of photonic devices was reduced to 0.115 nm. The wedge angle of the sidewall can be controllable from 10° to 55° [31].

The PLACE approach demonstrated in 2018 opened an avenue for wafer-scale, ultralow-loss photonic systems and devices [32,101,127], in which femtosecond laser micromachining was used for Cr mask patterning. Femtosecond laser lithography is not irreplaceable because one may use EBL, UV, or other optical lithography techniques to produce pattern

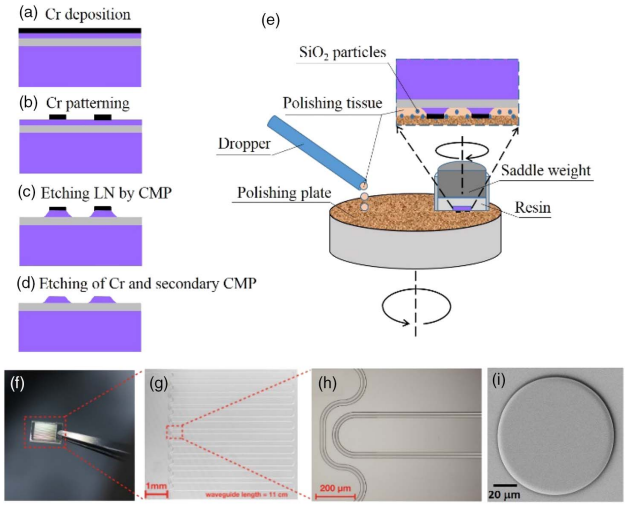

Fig. 5. (a)–(e) Schematic diagram of the fabrication process with PLACE [33]. (f) Camera photo, (g) optical microscope image, and (h) enlarged image of the fabricated 11-cm-long ridge waveguide with 0.027 dB/cm propagation loss [33]. (i) Microdisk with a Q factor of 4.7×10^7 [31].

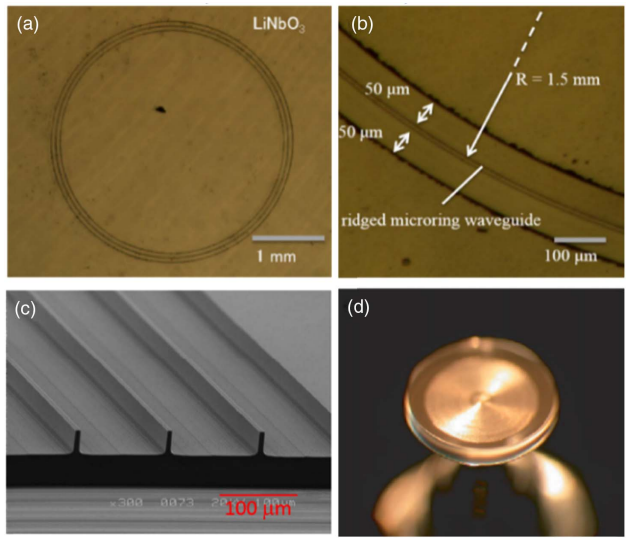

Fig. 6. (a) Ring resonator fabricated by ultra-precision cutting and (b) magnified image of (a) [139]. (c) Ridge waveguide fabricated by optical grade dicing [133]. (d) Disk resonator with a diameter of 3 mm fabricated by diamond polishing [108].

masks on Cr. Then the patterns can be transferred to the LNOI using the CMP. Considering the short history of the PLACE technique, these possibilities will be explored soon in the future. Another issue yet to be resolved is that the aspect ratio of the nanostructures fabricated with CMP is lower than 1.5 at the moment due to the limited selectivity of the metal mask and LN [31]. Fabricating coupled devices with a gap within 2 μm is difficult. Hence, much effort should be made to achieve higher aspect ratios critical for constructing high-density PICs.

D. Fabrication Techniques of Photonic Structures Without Lithographic Nanostructuring of the LNOI

Thin-film LN is hard for lithographic nanostructuring due to its low hardness and chemical inertness. Historically, some approaches avoiding the lithographic nanostructuring of the LNOI were developed to enable cost-effective fabrication of photonic devices on LN thin film with high optical quality.

One approach is based on mechanical fabrication methods, such as ultra-precision cutting [128,129], optical grade dicing [130–137], single-point diamond turning, and mechanical polishing [108,138]. Simple structures, such as a straight waveguide, curved waveguide with a relatively large curvature radius, and WGM microresonator [e.g., microring in Figs. 6(a) and 6(b)], can generally be fabricated individually using this approach. Accordingly, Takigawa *et al.* used ultra-precision cutting to fabricate ridge waveguides on both LN and LNOI. Typical ridge waveguides possess a top width of 5–8 μm, depth of 2.5–4.5 μm, taper angle of 88°, and minimum bending radius of 300 μm [128,129]. The propagation loss of the straight waveguide was 0.1 dB/cm at 1550 nm wavelength [128]. Figures 6(a) and 6(b) show a microring resonator fabricated on bulk LN. The RMS roughness of the sidewall was 4.5–6.1 nm, which was limited mainly by the available positioning accuracy of each translational axis and the rotational axis during each repeated cutting [128].

Optical grade dicing is a high-aspect-ratio (above 500) technique that typically has a sidewall angle of 88° similar to that of ultra-precision cutting. The top widths of waveguides as small as 1 μm and 2 μm were demonstrated on both bulk LN and LNOI [135,140], respectively. The minimum propagation losses of the ridge waveguides fabricated on the bulk LN and LN thin film were 0.2 dB/cm [133] and 0.3 dB/cm [137], respectively. Figure 6(c) shows a 1-cm-long proton-exchanged periodically poled MgO:LN ridge waveguide with an insertion loss of 3.2 dB. The ridge waveguide possesses 6 μm width and 30 μm depth [133]. Although low-loss ridged waveguides were achieved using precision machining, producing curved waveguides is impossible because the dicing blade can move along only a fixed direction.

Single-point diamond turning and mechanical polishing are used to individually fabricate ultrahigh-Q resonators [108]. The Q factor of a millimeter-scale resonator [Fig. 6(d)] is up to 2×10^8 [138,141–144]. An ultra-smooth sidewall can be achieved by diamond polishing. The minimum radius of the resonator can be as small as 35 μm [145]. However, diamond turning and mechanical polishing are not capable of fabricating on-chip photonic-integrated devices.

An alternative method for making photonic devices on the LNOI while avoiding dealing with the LN crystal was proposed and realized by bonding the LN film with a thin layer of lithographically patterned microstructures made from high-refractive index materials. This method is called the rib-loading approach, which circumvented the need to process LN. Therefore, mature fabrication techniques developed for semiconductor materials, such as silicon, GaAs, and InP, can be applied to produce LNOI devices. These materials, including plasma enhanced chemical vapour deposition (PECVD) silicon

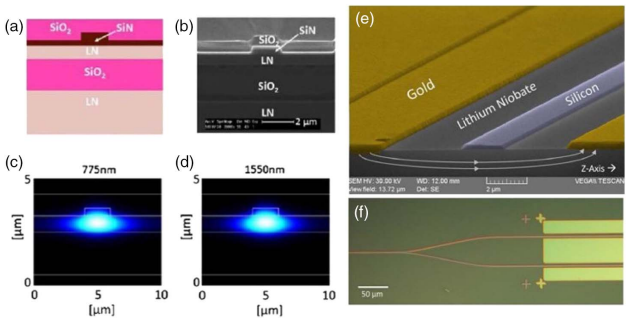

Fig. 7. Hybrid SiN ridge waveguide on the LNOI [146]. (a) Schematic cross section. (b) SEM image of the cross section. (c), (d) Simulated fundamental transverse electric (TE) mode profiles of the waveguide at 775 and 1550 nm, respectively. Hybrid silicon ridge waveguide on the LNOI [153]. (e) SEM image of the cross section of the Si–LN modulator. (f) Optical micrograph of the Y-junction and modulator electrodes.

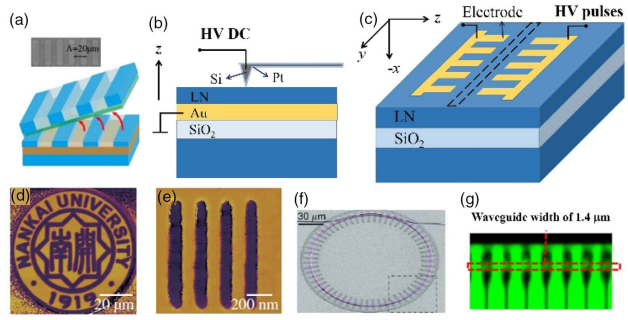

Fig. 8. (a) Schematic diagram of the ion slicing thin film from prepoled LN [130]. Inset: PPLN thin film. Schematic diagrams of the PPLN thin film fabricated by (b) atomic force microscope/piezoelectric force microscopy (AFM/PFM) poling method [164] and (c) microelectrode poling method [148] with a high-voltage (HV) direct-current (DC) source. PFM images of (d) logo of Nankai University and (e) PPLN strips with period of 200 nm width and a duty ratio of 50% [166]. (f) SEM image of a PPLN microring with EBL poling [113]. (g) Second-harmonic confocal microscopy of the PPLN thin film fabricated by microelectrode poling [54].

nitride (SiN) [146–148], silicon [70,149–153], chalcogenide glass (ChG) [154], tantalum pentoxide (Ta_2O_5) [29], and titanium dioxide (TiO_2) [155], were directly deposited or bonded on thin-film LN and fabricated into ridge waveguides using semiconductor processing techniques. Figures 7(a)–7(d) show a SiN rib waveguide on an LN thin film [146]. The modes were confined mainly in an LN thin film. Figures 7(e) and 7(f) illustrate an electro-optically tunable Y-junction integrated with electrodes, where a hybrid waveguide was formed by the Si ridge waveguide on an LN thin film [153]. However, some parts of the optical mode distribution were not located in LN, and the field confinement in LN was relatively weak [Figs. 7(c) and 7(d)], which will worsen the performances of the LNOI photonic devices. To fully use the superior material properties of LN and achieve the maximum electro-optical tuning efficiency and second-order optical nonlinearity, the confinement of modes in the waveguides directly patterned into the LNOI thin film is strongly in demand. Such waveguides can be fabricated using the techniques described in Sections 2.B and 2.C, which are becoming more and more mature today.

If the rib-loading material on the Z-cut LN thin film has a lower refractive index, certain transverse magnetic (TM) bound modes can be guided in LN without energy dissipation to the transverse electric (TE) continuous mode by careful dispersion engineering [156,157]. Polymers, such as electron-beam resist ZEP520A, were used to fabricate patterns of rib, disk, and ring shapes, to form the LN waveguide, microdisk, microring, Mach–Zehnder interferometer (MZI), and so on.

3. DOMAIN PATTERNING METHODS

As an important ferroelectric material, monocrystalline LN has a permanent electric dipole moment, which is called spontaneous polarization. This spontaneous polarization can be reversed by applying a electric field stronger than the so-called coercive field larger than 2 kV/cm for congruent LN at room temperature [25,158]. The coercive field can be varied by doping ions. During the domain reversion process, the sign of the electro-optic and effective second-order nonlinear optical coefficients is alternated with the domain inversion. Domain patterning, defined as patterning LN into oppositely oriented regions, is generally considered as the basis of the quasi-phase-matched optical frequency conversion. The crystal is named after periodically poled LN (PPLN). The domain patterning on an LN thin film can be performed in two fashions: (1) exfoliation of the LN thin film from an already periodically poled bulk crystal [130,159]; and (2) locally poling the LN thin film after the photonic structures are fabricated on the homogeneous LNOI substrates [113,116,160–167].

In the first method, domain patterning was conducted on the Z-cut bulk LN crystal by electrode poling [158], femtosecond laser irradiation [168], utilization of temperature fluctuations during Czochralski growth [169], and so on. The domain pattern usually has a relatively large spatial period typically larger than several micrometers due to the horizontal expansion of the domain in a thick LN wafer. Figure 8(a) shows an ion-sliced PPLN thin film bonded onto the silica layer coated on the LN substrate [130]. For the electro-optic applications of LNOI devices, the largest electro-optic coefficient (χ_{33}) was unavailable in this Z-cut PPLN thin film.

LN thin-film poling has been investigated in the past few years. The domain inversion generated by directly applying a strong electric field was found to be unstable when the thickness of the Z-cut LN thin film with an optic axis perpendicular to the LNOI surface was smaller than 1 μm [162,165]. To overcome this issue, atomic force microscope/piezoelectric force microscopy (AFM/PFM)-tip with high voltages was employed to pattern micro/nano-domains on the LNOI [160,164,166] [Fig. 8(b)]. In this method, an electrode layer is placed underneath the LN thin film, which may be helpful to obtain a stable domain pattern. With the aid of AFM, a two-dimensional domain patterning can be performed on the photonic devices on the LN film with a domain size down to 200 nm [Figs. 8(d) and 8(e)] [166] and biperiodic

poling [170]. Such fine domain structures enable not only the utilization of d_{33}, but also the compensation for a very large wavevector mismatch in nonlinear processes with counter-propagating light waves. Another method for domain patterning on a Z-cut thin film was based on EBL [113,171] [Fig. 8(f)]. The optic axis for the X-cut thin film lies in the thin film. Domain patterning can be performed by fabricating pairs of microelectrodes horizontally deposited on the X-cut LN thin film [148,167,172–175] [Figs. 8(c) and 8(g)]. The minimum gap between the two electrodes in each pair is often >0.6 μm [176], thereby requiring an applied voltage on the level of several hundred volts for the poling. The domain patterning should be aligned in the y direction to utilize χ_{33} and d_{33}. The metal microelectrodes are often fabricated by lithography and the etching/liftoff process [Fig. 8(f)][113].

4. PHOTONIC DEVICES FOR PICS

Due to the rapid development of microfabrication techniques, various types of LNOI devices with unprecedented performances and compact sizes were recently demonstrated. Tables 1 and 2 present waveguide propagation losses and loaded Q factors of microcavities fabricated on the LNOI with different techniques, respectively. The losses in the waveguide and the Q factors in the microcavities remarkably reached ~0.03 dB/cm [33,34] and 4.7×10^7 [31], respectively. The waveguides and microcavities are the building blocks for constructing LNOI photonic-integrated devices with a broad range of functionalities.

A. Electro-Optic Modulators and Acoustic Optics

The linear electro-optical effect of LN, which is known as the Pockels effect, enables high-speed and efficient tuning of the

Table 1. Propagation Losses of Waveguides Fabricated with Different Techniques (SM, single mode)

Device	Loss/(dB/cm)	Wavelength/nm	Fabrication Technique	Source
Ridge waveguide	61	1550	Wet etching	LNOI 2015 [89]
Ridge waveguide	9.9 TM, 12.9 TE	1550	Ar ion milling	LNOI 2009 [159]
Ridge waveguide	5	1550	Ar ion milling	LNOI 2016 [177]
Ridge waveguide	1.3 TM, 0.268 TE	1550	Ar ion milling	LNOI 2018 [178]
Ridge waveguide	3	1550	Ar ion milling	LNOI 2018 [179]
Ridge waveguide	0.41 TE	1550	RIE	LNOI 2018 [180]
Ridge waveguide	0.04 TE	1500	RIE and CMP	LNOI 2018 [125]
Ridge waveguide	0.027	1590	Ar ion milling	LNOI 2018 [34]
SM ridge waveguide	0.06	637	Ar ion milling	LNOI 2019 [181]
SM ridge waveguide	3 TE	1550	Ar ion milling	LNOI 2019 [69]
Ridge waveguide	0.027 TE	1560	PLACE	LNOI 2018 [33]
SM ridge waveguide	0.042	1550	PLACE	LNOI 2019 [126]
SM ridge waveguide	0.029	1550	PLACE	LNOI 2020 [32,182]
Ridge waveguide	0.5	1550	Dicing	LNOI 2011 [140]
Ridge waveguide	2.1 TM, 2.0 TE	1550	Dicing	LNOI 2018 [134]
Ridge waveguide	0.3	1550	Dicing	Thin film PPLN 2019 [137]
Hybrid TiO_2–LN waveguide	14 TM, 5.8 TE	1550	Etching-less	LNOI 2015 [183]
Hybrid Si–LN waveguide	0.3	1530	Etching-less	Thin film PPLN 2016 [148]

Table 2. Loaded Q Factors of WGM Microresonators and PhC Cavities

WGM	Loaded Q Factor	Wavelength/nm	Fabrication Technique	Source
Microring	4×10^3	1555	Ar ion milling	LNOI 2007 [30]
Microdisk	1.02×10^5	1507	Ar ion milling	LNOI 2014 [38]
Microdisk	1.19×10^6	1549	Ar ion milling	LNOI 2015 [37]
Microdisk	3×10^6	976	RIE, CMP	LNOI 2017 [100]
Microdisk	6.7×10^5	1550	RIE	Thin film PPLN 2018 [160]
Microring	1.3×10^6	1550	RIE, CMP	Thin film PPLN 2018 [184]
Microring	1.3×10^6	1493	Ar ion milling	LNOI 2018 [185]
Chaotic disk	1.5×10^6	1551	Ar ion milling	LNOI 2018 [122]
Microring	5×10^6	1590	Ar ion milling	LNOI 2018 [34]
Microring	1.78×10^6	1572.6	ICP RIE	LNOI 2019 [186]
Microdisk	2.5×10^5	1554	Femtosecond, FIB	LNOI 2014 [35,39]
Microdisk	1.84×10^6	1548	Femtosecond, FIB	LNOI 2018 [187]
Microdisk	9.61×10^6	1547.8	Femtosecond, FIB	LNOI 2019 [51]
Microdisk	1.46×10^7	773	PLACE	LNOI 2018 [103]
Microring	5×10^6	1560	PLACE	LNOI 2018 [33]
Microdisk	4.7×10^7	1542	PLACE	LNOI 2019 [31]
PhC	5.35×10^2	1350	FIB	LNOI 2013 [104]
PhC	1.1×10^5	1450	Ar ion milling	LNOI 2017 [41]
PhC	5.43×10^4	1505	Ar ion milling	LNOI 2018 [188]
PhC	1.41×10^6	1564.4	Ar ion milling	LNOI 2019 [114]

refractive index of LN and the linear optical properties of LN waveguides, WGM microresonators, and PhC cavities [32,45,64,150,189–197]. The fast electrical tuning of the optical properties of LN devices is useful in applications involving electro-optical modulators and switches. Before the LNOI invention, LN electro-optical devices were based mostly on weakly confined channel waveguides formed by proton exchange or Ti diffusion technologies [198]. The energy distribution of the waveguide mode is similar to that of the single-mode fiber due to the relatively low refractive index contrast between the core and cladding of weak LN waveguides. Therefore, the gap between the adjacent electrodes of the electro-optical modulator based on weak LN waveguides is often more than 30 μm to avoid metal absorption. As a result, this leads to low modulation efficiency and a large electrode length [66].

Benefiting from the high refractive index contrast and the compact size of wire/ridge waveguides, the distance between the electrodes on the opposite sides of the waveguide can be reduced to several micrometers. Therefore, the driving voltage can be significantly reduced to a level compatible to the output of the CMOS signal generator. Optimizing the layout and parameters of the photonic structures integrated with electrodes allows the velocity match between the light propagating in the waveguide and the microwave in the electrode to be shrunk by an order of magnitude, thereby reducing the fabrication cost and difficulty. For these reasons, the investigation on the electro-optical modulation on the LNOI has attracted much attention after the LNOI invention.

1. Microresonator-Based Electro-Optic Modulators

The resonant wavelength tunability of microresonators is important for many photonic applications [30,37,150,189,193,194,196,199–201]. In 2007, Guarino *et al.* demonstrated electro-optically controllable microring resonators in a Z-cut LNOI film, where two parallel planar electrodes were added on a chip with ~3.4 μm space. These resonators showed a tunability of 0.14 GHz/V [30]. In 2015, Wang *et al.* achieved an effective tunability of 3.0 GHz/V by applying voltage to the external indium tin oxide (ITO) electrodes sandwiched with free-standing high-Q (1.19×10^6) microdisk resonators [Figs. 9(a) and 9(b)] [37]. In 2017, the monolithic electro-optic tuning of an on-chip LN microdisk resonator was demonstrated by integrated in-plane microelectrodes with a microdisk [Fig. 9(c)]. The microdisk was placed in the center of the gap between two microelectrodes. Consequently, a high electro-optical tuning coefficient of 3.41 pm/V was obtained due to the narrow gap (75 μm) [199]. A higher electro-optic tuning rate of 29.2 pm/V was recently demonstrated with a more compact and efficient pattern of the microelectrodes surrounding the microdisk. The pair of microelectrodes consisted of a pad-shaped electrode placed in the microdisk surface and a ring-shaped electrode underneath the disk with ~2 μm space. An electro-optic tuning rate of 29.2 pm/V was achieved when the horizontal gap between the electrodes was 1 μm [202] [Figs. 9(d)–9(f)] [201]. More recently, the impact of the waveguide curvature on the tuning efficiency of a microring in an X-cut LNOI and the response was well analyzed and derived by Bahadori *et al.* [203].

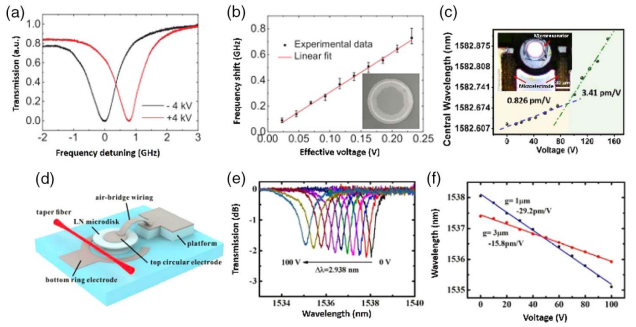

Fig. 9. Electro-optically tunable microresonator. (a) Resonant frequency shift with external voltage [37] showing (b) effective efficiency of 3.0 GHz/V. (c) Microdisk integrated with microelectrodes with a tuning efficiency of 3.41 pm/V [199]. (d)–(f) Microdisk integrated with compact out-of-plane microelectrodes with 1 μm gap showing a high efficiency of 29.2 pm/V [202].

The tuning efficiency of the WGM microresonator was much higher than that in the ridge waveguide and the Mach–Zehnder modulator (MZM) due to a high-Q factor. Therefore, a ring modulator was used to generate an electro-optic frequency comb [62] (Section 4.B.3) and form a microwave-to-optical converter [204] (Section 4.C.6). The ring modulator has a more compact footprint than the MZM; however, its bandwidth is limited by the Q factor of the WGM. A high-speed electro-optic modulator was also demonstrated by Li *et al.* in a tiny PhC. It exhibited a high tuning efficiency of 1.98 GHz/V and a broad bandwidth of 17.5 GHz with a very low bit-switching energy of 22 fJ [197].

2. High-Speed Mach–Zehnder Interferometer Electro-Optic Modulator

Monolithic high-speed electro-optic modulators [191] based on the MZI with integrated electrodes were demonstrated in X-cut LNOI devices covered with a SiO_2 cladding layer [44,179,204,205]. A 5:5 Y-junction beam splitter split the optical signal into two LN ridge waveguides that served as two arms of the MZI. The signals were then combined with other Y-junctions [Figs. 10(a)–10(d)]. The metal electrodes were designed close to the waveguide with a space <2.5 μm to achieve a high electro-optical efficiency without substantially increasing the optical losses. The SiO_2 layer thickness was designed to be 4.7 μm to achieve velocity matching between microwave and optical wave. The electrode structure was also optimized, such that the group refractive indices for the microwave and optical wave were both approximately 2.2, and the transmission line impedance was near 50 Ω. A high-frequency microwave with a group velocity matched with the optical field induces the optical phase difference between two arms through the Pockels effect. The optical signal transmission varied from maximum to minimum when the phase difference was tuned from zero to π. Benefiting from the significantly increased spatial overlap between the tightly confined optical and microwave modes, a 1.4 V half-wave voltage and a 2.8 V · cm half-wave voltage length product were achieved. Therefore, the microwave signal driven by a CMOS circuit could be directly applied on the electrodes, enabling a chip-level integration with low-cost

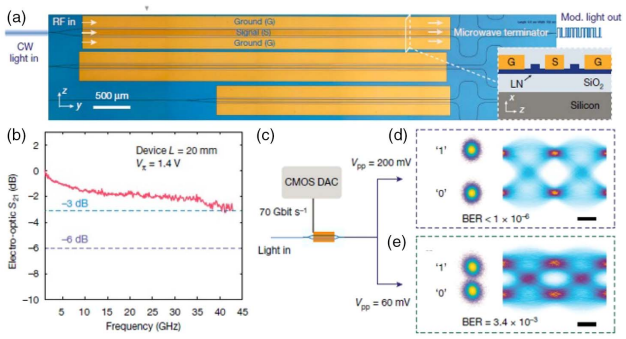

Fig. 10. (a) Micrograph of the electro-modulator chip consisting of three MZI modulators. Inset: cross-sectional schematic of the modulator. (b) Data-transmission experiments at 70 Gbit/s rate in the modulator driven by (c) CMOS circuit. Measured constellation diagrams obtained with a coherent receiver (left) and reconstructed eye diagrams (right) at peak-to-peak voltages of (d) 200 mV and (e) 60 mV [44].

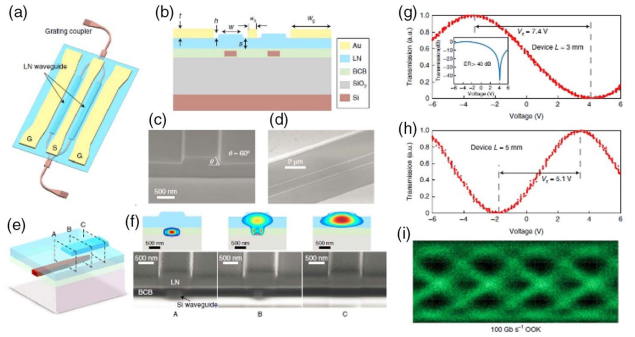

Fig. 11. (a) Schematic of a Si–LN hybrid modulator. (b) Cross section of the Si–LN hybrid waveguide. SEM images of (c) cross section of the LN ridge waveguide and (d) electrodes and the LN waveguide. (e) Schematic of the VAC. (f) SEM images of the cross sections of the VAC at different positions (A, B, and C) and calculated TE mode distributions. Normalized transmission of the devices with (g) 3 mm and (h) 5 mm lengths as a function of the applied voltage showing half-wave voltages of 7.4 V and 5.1 V, respectively. Inset: measured extinction ratio on a logarithmic scale. (i) Optical eye diagrams for the OOK signal at data rates of 100 Gbit/s [71].

microwave sources. The electro-optic response showed a 3 dB bandwidth >45 GHz. The extinction ratio was measured to be as high as 30 dB. The data rate of 210 Gbit/s in the case of 8-ASK was demonstrated in the modulator with 100 GHz tuning speed. The overall on-chip phase-shifter insertion loss was less than 0.5 dB due to the low propagation loss of 0.2 dB/cm. This high-speed modulator possessed a smaller footprint, higher bandwidth, and much lower half-wave voltage compared with the electro-optic modulator on bulk LN. The in-phase/quadrature electro-optic modulator encoding information on both the amplitude and the light phase is required to achieve a large bandwidth. The modulation formats for signal encoding, including quadrature phase-shift keying and quadrature amplitude modulation, were demonstrated on an LNOI platform, showing modulation speeds up to 220 Gbit/s (110 Gbaud) and 320 Gbit/s (80 Gbaud), respectively [45].

3. Hybrid MZI Electro-Optic Modulator

In addition to the LNOI, hybrid platforms, where a high refractive index material (e.g., Si, SiN, and ChGs) layer is bonded to LN thin film, were also used to produce LN electro-optical modulators and showed promising results [46,47,70,150,151,154,190,193–196,206–211]. In 2016, a hybrid MZI modulator with 8-mm-long SiN-waveguide arms on an LN thin film was demonstrated with a half-wave voltage length product of 3.1 V · cm at DC and 6.5 V · cm up to 50 GHz RF due to the narrow electrode gap of 5.5 μm [70]. More recently, a half-wave voltage length product as low as 2.11 V · cm was demonstrated on a hybrid Si_3N_4–LN electro-optic MZI modulator [195]. This value was lower than the reported results of the monolithic LN modulators [44]. The modulator possessed a low DC half-wave voltage of only 0.875 V with an interaction region length of 2.4 cm and a high power extinction ratio of approximately 30 dB. However, these hybrid platforms may ultimately be limited by lower modulation efficiency and smaller optical confinement in the LN crystal due to the introduction of other materials with a high refractive index. In 2019, a hybrid Si–LN MZI modulator was presented by utilizing two layers of hybrid integrated Si–LN ridge waveguides and vertical adiabatic couplers (VACs) [71] (Fig. 11). The optical signal was split by a silicon-waveguide Y-junction beam splitter, transferred fully into two LN-waveguide arms by VACs, and similarly transferred back into the silicon-waveguide Y-junction combiner. The propagation loss of the LN waveguides was 0.98 dB/cm. Electrodes with 6.5 μm gap were fabricated near both sides of the LN waveguide without a SiO_2 cladding layer. The half-wave voltage length product was only 2.2 V · cm with 40 dB extinction ratio due to the narrow gap and efficient electro-optical coupling. Subsequently, 2.5 dB insertion loss, at least 70 GHz electro-optic bandwidth, and up to 112 Gbit/s four-level pulse amplitude modulation (PAM-4) were demonstrated on this hybrid Si–LN MZI modulator.

4. Cascaded MZI Electro-Optic Modulator

The extinction ratio of a single MZI modulator highly depends on Y-junctions with a strict 50:50 splitting ratio. However, the fabrication of Y-junctions with a perfect 50:50 splitting ratio is difficult, impossible even, due to the fabrication error. Cascaded MZIs were used to overcome this problem in spite of the fabrication error, providing a higher extinction ratio of 53 dB [69,212].

A beam splitter with a 50:50 splitting ratio was demonstrated using two electro-optic MZIs sandwiched with an electro-optic phase shifter on an X-cut LNOI [126]. The half-wave voltage of the phase shifter was 6.7 V for the TE mode. The beam splitting ratio of the beam splitter was tuned to 50:50, even though the origin splitting ratio of the directional coupler was in the 85:15 to 15:85 range [212]. The extinction ratio was 40 dB at 1550 nm wavelength. When this beam splitter is connected with two output arms of different lengths, the propagation loss can be inferred from the difference between the output powers measured as 0.042 dB/cm of the TE mode by comparing the output powers. A multifunctional beam splitter consisting of seven MZIs and four phase shifters was fabricated based on single-mode ridge waveguides on an

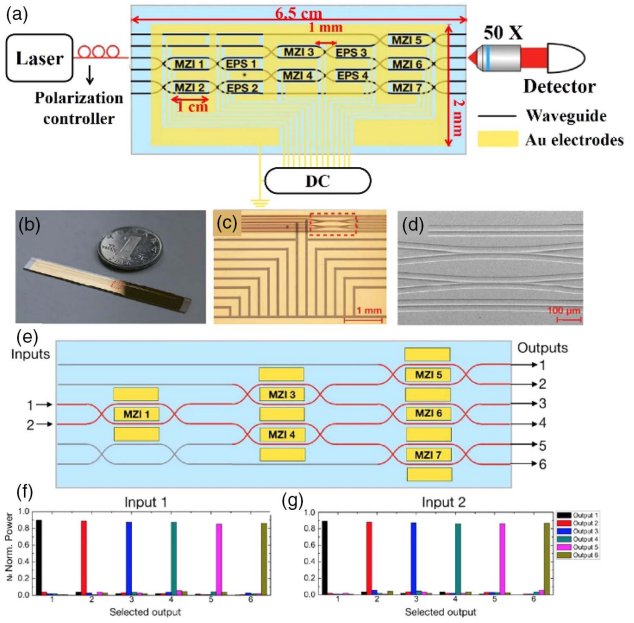

Fig. 12. Large-scale beam splitter [102]. (a) Schematic of the multifunctional beam splitter. (b) Photo image of the photonic chip. (c) Optical micrograph of the region in the red dashed box in (a). (d) SEM image of the region in the red dashed box in (c) before electrode fabrication. (e) Schematic of the 1 × 6 switch. Normalized output power switching from input ports (f) 1 and (g) 2 to output ports 1 to 6.

X-cut LNOI fabricated by PLACE [102]. The extinction ratio was 28 dB. Functions such as a 1 × 6 optical switch and balanced 3 × 3 interferometer, were demonstrated by reconfiguring the electrode array integrated with the beam shifter (Fig. 12). The electro-optic beam splitter can be used for the optical neural network, photon manipulation, and programmable photonic signal processing.

A monolithically integrated 1 × 4 reconfigurable electro-optic tunable interleaver consisting of three asymmetrical MZIs was produced in an X-cut LN thin-film sample by Ar ion milling [213] (Fig. 13). Each MZI was sandwiched between two different 3 dB multimode interferometers (MMIs). The average insertion losses of ∼20 dB (∼21 dB) and extinction ratios of 8–15 dB (7–13 dB) were measured when inputting the TE (TM) polarized light. The device exhibited a polarization-insensitive center wavelength and channel spacing of ∼50 GHz in a wide wavelength range from 1530 nm to 1605 nm. The minimum switching voltage was 4.5 V, and the maximum channel isolation was ∼15 dB, showing potential for application in dense wavelength-division multiplexing (WDM) optical networks.

5. Michelson Interferometer Modulator

Compared with the MZI, the Michelson interferometer modulator (MIM) possesses reflective mirrors on both arms; thus, the interaction length between the light wave and the modulating electrical field is doubled. The MIM can efficiently enhance the modulation efficiency and/or reduce the device size compared with the MZI modulator. An on-chip MIM was demonstrated on an X-cut LN thin film by Ar ion milling [214].

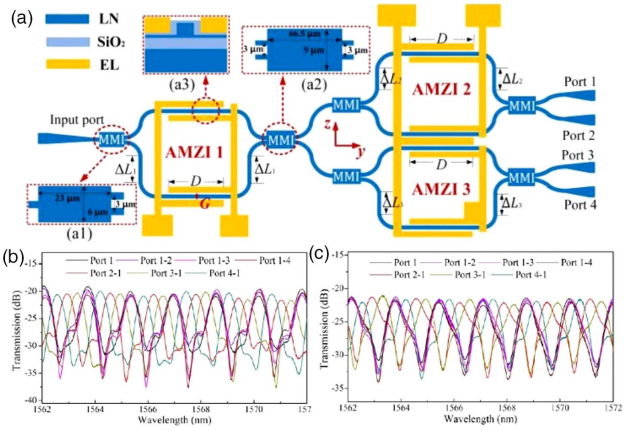

Fig. 13. Electro-optic tunable interleaver [213]. (a) Schematic of the reconfigurable 1 × 4 electro-optic tunable interleaver in an X-cut LN thin film. Measured wavelength switching ports 1 – i and i – 1 of the interleaver for (b) TE- and (c) TM-polarized input light.

This MIM included a 50:50 TE split 2 × 2 MMI coupler, a two-arm phase shifter, and two reflected broadband loop mirrors. The propagation loss of the waveguide was 4.6 dB/cm. The half-wave voltage length product of 1.4 V · cm was obtained in this MIM, which was less than the state-of-the-art half-wave voltage length product of 1.7 V · cm for the MZI modulator [44,71]. However, the electro-optic bandwidth was limited to 12 GHz due to the velocity mismatch between optics and microwave.

6. Acoustic–Optical Devices

LN possesses a large electromechanical coupling coefficient for connecting light, motion, and microwave due to its excellent properties of low loss, large electro-optic coefficients, and piezoelectric effect [48,215–217]. The surface acoustic wave (SAW) in a piezoelectric crystal is an elastic wave with an electric field component. The SAW generated by an interdigital transducer modulates the effective refractive index of light traveling in piezoelectric photonic devices (e.g., MZI [48,117], microcavity [48,117,218], and waveguide) [49,219]. In 2019, an on-chip acousto-optic modulator was first reported by Cai *et al.* on the LNOI [117] with an effective photoelastic coefficient of 0.053. The strong piezoelectricity and electro-optic effects of LN in conjunction with the photoelastic effect will enable a strong microwave-to-acoustic coupling. Accordingly, the microwave-to-optical conversion [48] was studied by Shao *et al.* on an MZI and a high-Q racetrack resonator, each integrated with a suspended acoustic resonator on a thin-film LN and showing a half-wavelength product as low as 0.046 V · cm at the acoustic mode around 3.3 GHz and a strong acousto-optic coupling strength of 1.1 kHz, respectively. A lossless microwave-photonic link was demonstrated on the racetrack resonator with ∼50 mW optical power routing. A high-Q PhC resonator on the LNOI was used to achieve acoustic–optical coupling with an optomechanical coupling rate of 120 kHz by optimizing the device parameters. Phonon lasing was observed using a blue-detuned pump laser [50].

B. Nonlinear Optical Light Sources

1. Second-Order Nonlinear Optical Light Source and Frequency Comb

LN provides an excellent platform for a nonlinear optical study and applications benefiting from its giant nonlinear optical coefficients and broad transparent window. The light field can be limited in a small volume due to the small mode volume of the LN waveguide/microresonator on the LNOI, which enhances the light intensity. A high-Q LN microresonator can further enhance light intensity due to the light confinement in time, which is beneficial for nonlinear optical process. Both second- [e.g., second-harmonic generation (SHG), sum-frequency generation (SFG), and parametric down conversion (PDC)] and third-order [e.g., four wave mixing (FWM) and Raman effect] nonlinear optical effects were demonstrated in photonic devices on the LNOI. These nonlinear optical processes are crucial for accessing the new frequency of classical optics and on-chip quantum light sources for quantum information processing [17,18].

For optical parametric processes, the energy and momentum conversation conditions must be satisfied simultaneously. Therefore, phase matching is a crucial factor that cannot be avoided for the parametric processes in LN devices not only in bulk form, but also on a chip. The phase matching mechanics in WGM resonators was reviewed by Lin *et al.* [220]. According to our point of view, phase mechanics can be roughly classified into modal phase matching (MPM), cyclic phase matching (CPM), quasi-phase matching (QPM), and natural QPM (NQPM). Second-order nonlinear optical effects in LNOI microcavities and ridge waveguides were already reviewed by several papers [26,220–224]. Hence, we focus herein only on the important progresses made recently.

SHG with a high efficiency up to 1.5%/mW, PDC, and SFG were demonstrated in Z-cut microdisks and microrings using the MPM [52,112,225]. Modal-phased-matched SHG and PDC were also demonstrated in the LNOI ridge [226] and hybrid [227,228] waveguides. Moreover, SHG with a conversion efficiency of 1.106×10^{-3}/mW was also demonstrated in an X-cut microdisk, and broadband spontaneous PDC was exhibited using the CPM [53,229]. However, the largest nonlinear coefficient d_{33} of LN, which is almost one order of magnitude higher than other coefficients, is unavailable when utilizing the MPM and the CPM.

The periodical inversion of the sign of the effective nonlinear coefficient with the period of twice the coherent buildup length of a nonlinear interaction is needed when using d_{33}. This provides an additional reciprocal vector to compensate for the phase mismatching. This phase matching scheme is well known as the QPM. Since 2009, PPLN X-cut ridge waveguides have been fabricated for SHG, PDC, and different frequency generation [54,56,146,148,167,230–234]. The record-high normalized conversion efficiency of SHG is 3061%/$(\mathrm{W}\cdot\mathrm{cm}^2)$ [54]. Entangled photon pairs [56,117,171,172] were also demonstrated on thin-film PPLN ridge waveguides. Entangled photon pairs at 1570 nm wavelength with high coincidence-to-accidental count ratio (CAR) >67,000 (when the pair coincidence rate is $7.6 \pm 2.6 \times 10^4$ pairs/s), two-photon interference visibility $V > 99\%$, and heralded single-photon autocorrelation $g_H^2(0) < 0.025$ were observed in an X-cut PPLN ridge waveguide [172]. The brightness was 4.6×10^5 pairs/(s · GHz · mW).

The theory of the QPM in the LN resonator was proposed in 2003 [235]. Linearly poled microdisks and a microring with a straight strip-shaped domain were first demonstrated in 2018 for SHG without d_{33} utilization due to the difficulty in radial poling. In 2019, a linearly poled racetrack X-cut microresonator was utilized to generate SHG using d_{33} with an ultrahigh conversion efficiency of 230%/mW [116]. A radially poled Z-cut microdisk [166] and a microring [113] were later successfully fabricated with an ultrahigh conversion efficiency of 250%/mW. A double periodically poled LNOI microdisk was first fabricated by Zhang *et al.* to generate cascaded nonlinear processes, such as SHG, third-harmonic generation (THG), and fourth-harmonic generation, which resulted from the multiple reciprocal vectors providing from biperiodic poling [236]. Unfortunately, the LN devices made from the PPLN suffered from an increased scattering loss due to the additional surface and the inner inhomogeneity near the domain wall. As reported, a 5 nm surface roughness resulting from the anisotropic HF etching for the $+Z$ and $-Z$ faces of LN to form the silica pillar was observed on a PPLN microdisk [160]. Therefore, the PPLN microresonator and the waveguide usually have relatively low qualities in loss compared with their monocrystalline counterparts.

The NQPM [51], which utilizes d_{33} in monocrystalline LN without poling, was demonstrated in an X-cut LN microdisk with 29.92 μm diameter, where all the waves (with wavelengths of 1548 nm, 774 nm, and 516 nm) participating in the nonlinear process were TE-polarized (Fig. 14). The sign of the effective nonlinear coefficient d_{eff} inverts periodically as light propagates along the microdisk periphery. The amplitude of

$$d_{\mathrm{eff}} = -d_{22}\cos 3\theta + 3d_{31}\cos 2\theta + d_{33}\sin 3\theta \quad \textbf{(1)}$$

oscillates as well, as shown in Fig. 14(b). The phase mismatching for SHG and THG was compensated for by the first and third Fourier components K_i of the nonlinear susceptibility d_{eff}, respectively [Fig. 14(c)]. A type-0 phase matching (eee) was achieved in the absence of domain patterning.

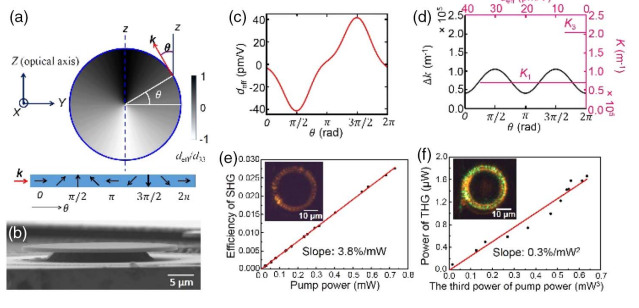

Fig. 14. SHG and cascaded THG based on the NQPM using d_{33} in an X-cut LN microdisk [51]. (a) Schematic of the NQPM. (b) SEM image of the X-cut microdisk. (c) d_{eff} at every azimuth angle θ. (d) Left: phase mismatching Δk; and right: positive Fourier components of d_{eff}. (e) Conversion efficiency as a function of the pump power. Inset: optical micrograph of SHG from the top surface of the microdisk. (f) Power of the THG as a function of the cubic power of the pump power. Inset: optical micrograph of THG.

The conversion efficiency reached 10%/mW, due to the fabrication of the LN microdisk resonator with Q factors $\sim 10^7$ and the employment of d_{33}. A highly efficient cascaded third harmonic was also generated with $1\%/\mathrm{mW}^2$ efficiency. The average SHG gain in a round trip was half that in the PPLN counterpart. However, the phase mismatching was not constant, but oscillated on a round trip, allowing a large phase matching spectral bandwidth. Highly efficient SHG and THG were observed at several pumped wavelengths when the pumped wavelength was tuned from 1530 to 1570 nm.

2. Frequency Combs on Third-Order Nonlinear Effects

The frequency comb is a kind of pulsed light source with equally spaced frequency components, which have applications in precision timing, optical communication, and spectroscopy. Traditionally, frequency combs are achieved by actively locking femtosecond lasers [237] or by a cascaded electro-optic modulation of continuous light sources. Cascaded FWM processes (Kerr effect) in high-Q microresonators were recently developed to generate a frequency comb on a chip benefiting from the dramatically enhanced light intensity inside a microresonator [238,239]. The microcavity frequency comb is featured with tens or even hundreds of gigahertz repetition frequency and dramatically reduced size and energy cost. Although the zero and repetition frequencies of light pulses generated in microcavities are usually unlocked, colleagues in this field are accustomed to calling them "frequency combs." We will also use the term "frequency comb" to describe the multiple frequency light sources obtained in LN microcavities.

An anomalous dispersion circumstance is usually needed in a microresonator to balance the Kerr effect and generate a frequency comb [240]. The Kerr frequency comb was initially demonstrated in an X-cut LNOI microring [60]. Mode-locked soliton microcombs were generated in Z-cut microrings with 100 μm radius and 600 nm thickness [58] (Fig. 15). This microring with a loaded optical Q factor of 2.2×10^6 and a free-spectral range (FSR) of 199.7 GHz has an anomalous group-velocity dispersion of $-D_2/(2\pi) = 1.76$ MHz in the

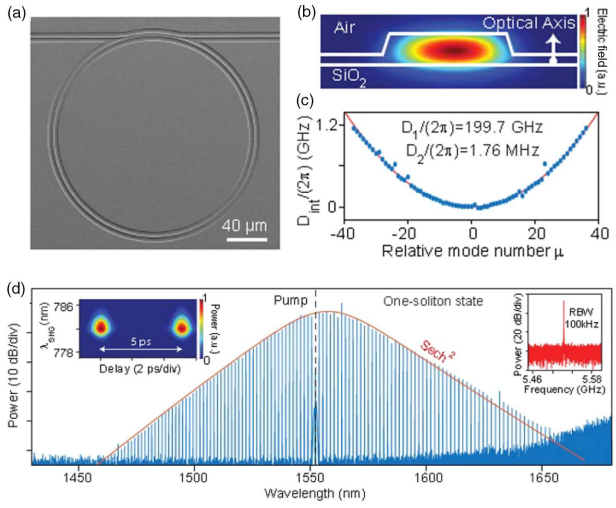

Fig. 15. Soliton frequency comb generating a microring [58]. (a) SEM image of the microring. (b) Cross-sectional schematic of mode. (c) Group-velocity dispersion. (d) Soliton comb.

telecom band. Laser scanning along the red side of the mode resonance is usually required in silica, Si_3N_4, CaF_2, and MgF_2 microresonators to drive the transition from a chaotic to a soliton state and overcome the thermal effect. The photorefractive effect [241] in LN causes an intensity-dependent decrease in the refractive index, which is opposite to the thermal effect, and the thermo-optic coefficient of the ordinary polarization is relatively small around room temperature; hence, the quasi-TE modes in the Z-cut microring will exhibit an optical bistability that stabilizes laser cavity detuning when the pump is red-detuned, where the soliton is formed, and enables the soliton mode-locking process to self-start, regardless of the direction of the pump laser wavelength. An output comb spectrum with a smooth sech^2-shaped spectral envelope indicating a single-soliton state was observed, where a 3 dB bandwidth was 27.9 nm, when the red-tuned pump laser power on the chip was 33 mW [Fig. 15(d)]. The temporal waveform of the output pulses was characterized by frequency-resolved optical gating to verify the single-soliton state, indicating pulse waveforms with a period of 5 ps. This value corresponds to the round-trip time of the microresonator. Additionally, the SHG of Kerr solitons was observed in the same ring, generating a visible Kerr soliton. The bi-chromatic soliton microcombs observed in the LNOI microresonator have great potential for on-chip self-referenced octave-bandwidth frequency-comb sources. The microcomb mode-locking operation to the 2 μm regime was also demonstrated in a Z-cut LN microring with 100 μm radius [57].

LN is a Raman-active crystal with several strong vibrational phonon branches [242–244]. Raman scattering allows Raman lasing [245] and Raman-assisted frequency combs [246,247]. Raman scattering was demonstrated on LN microresonators [100,103,248,249]. Furthermore, a Raman-assisted frequency comb with electro-optic tuning features was demonstrated in a Z-cut microdisk with 100 μm diameter and 800 nm thickness [250] (Fig. 16). This frequency comb was generated based on the Raman-assisted FWM at the red-tuned wavelength near the resonant wavelength [246,247]. The Q factor was $\sim 7.1 \times 10^6$, leading to a microcomb spanning over a spectral bandwidth of ~200 nm at a pump power as low as 20.4 mW [Fig. 16(e)]. The Z-cut microdisk was integrated with microelectrodes, based on which the electro-optical tuning of the comb with 400 pm spectral range and ~38 pm/100 V tuning efficiency was demonstrated [Fig. 16(f)]. A soliton Raman frequency comb was also demonstrated in an X-cut ridge waveguide microresonator [251]. This kind of frequency comb paved the way for electro-optical tuning octave-spanning frequency-comb spanning [247].

3. $\chi^{(2)}$ Frequency Comb on Optical Parametric Down Conversion and Electro-Optic Modulation

Aside from being realized based on third-order nonlinear optical effects, frequency combs can also be realized based on second-order nonlinear optical effects, such as cascaded wavelength conversion effects and electro-optic modulations. The $\chi^{(2)}$ frequency-comb generation [252] was demonstrated in a high-Q MgO-doped PPLN channel waveguide Fabry–Perot (FP) resonator through the PDC process [59]. This PPLN resonator was poled for quasi-phase-matched optical PDC from 1030 nm to 2060 nm wavelength. The resonator

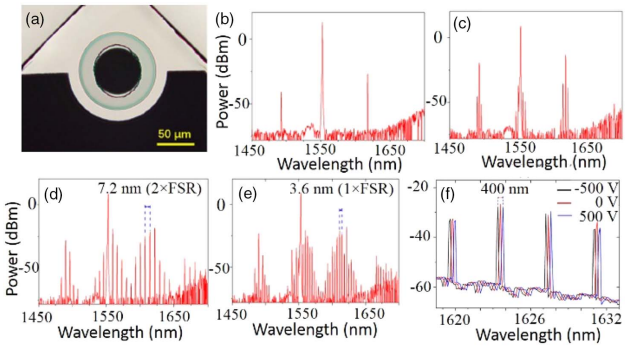

Fig. 16. Electro-optically tunable Raman-assisted frequency comb [250]. (a) SEM image of the microdisk integrated with Cr electrodes (black region). (b) Stokes and anti-Stokes Raman scatterings when pumping at 1552.39 nm wavelength before comb generation. (c) Raman-assisted FWM when pumping at 1552.68 nm wavelength. Comb generation with the spectral space of (d) double FSR of 7.2 nm and (e) single FSR of 3.6 nm when pumping at 1552.72 nm and 1552.74 nm wavelengths, respectively. (f) Electro-optic shifter of the comb line.

possessing a high-Q factor of 2.0×10^7 was coated for resonance around 2060 nm and anti-reflection at 1030 nm. The resonator was placed on a double-enclosed metal mount for temperature stability with sub-milli-Kelvin. The maximum conversion efficiency of the parametric light was 9.0% at a 1.0 W pump. The maximum output power was 0.37 W when the pump power was 9.1 W. The frequency comb was observed at both degenerate and nondegenerate wavelengths with spans of approximately 20 nm and 250 nm, respectively, around 2060 nm by slightly adjusting the resonator temperature [Figs. 17(a) and 17(b)].

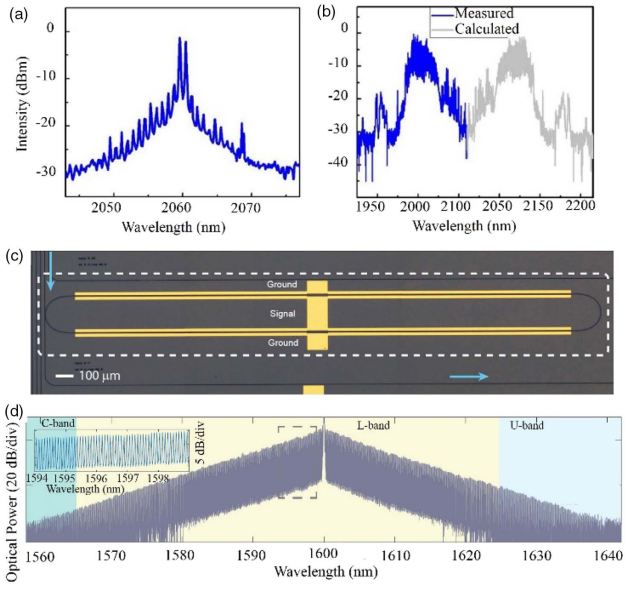

Fig. 17. $\chi^{(2)}$ frequency comb observed at (a) degenerate and (b) nondegenerate wavelengths [59]. (c) Micrograph of an electro-optically tunable microring for the electro-optic comb and (d) measured output spectrum of the comb [62].

The electro-optic frequency comb, which is also one kind of $\chi^{(2)}$ frequency comb, is traditionally formed by a series of phase and amplitude electro-optic modulators assisted with amplifiers, filters, and dispersion control devices. The electro-optic frequency comb was recently demonstrated in an LN resonator [253], LNOI racetrack microresonator [62,254], single waveguide [255], FP resonator formed by a distributed Bragg reflector [256], and cascaded MZM integrated with a phase modulator [61]. The broadband frequency comb relied on a high-Q microresonator, strong electro-optic interaction, and modulation frequency matching the FSR of the resonator. Thus, the optical sidebands generated by the phase modulator were resonant with the high-Q modes and cascaded, resulting in many comb lines spaced at the modulation frequency. The loaded Q of the racetrack microresonator was 1.5×10^6. The gap between the microelectrodes was 8 μm, ensuring efficient microwave delivery for achieving a strong phase modulation. The electro-optic frequency comb was generated with over 900 unique frequencies spaced by 10.453 GHz spanning 80 nm around 1600 nm by modulating the microresonator with the external microwave synthesizer with 10 V peak voltage at a frequency near the FSR [62] [Figs. 17(c) and 17(d)]. A higher Q factor was required to enable octave-spanning electro-optic comb generators. The optical frequency-comb generation with 16.3 GHz frequency spacing was realized using the FP cavity with a loaded $Q \sim 4 \times 10^5$ and a 4-mm-long modulation region [256]. Resonant driving may be another method to improve the performance of the LNOI electro-optic frequency combs [253]. However, the integrated device requires a much lower voltage and generates a broader comb-spanning range compared with the result of the bulk LN resonator [253].

4. Supercontinuum Generation

Supercontinuum generation (SCG) [257] with coherent octave spanning is often used to detect and stabilize the carrier–envelope offset f_{ceo} frequency through self-referenced interferometry for the frequency comb. It is usually realized by launching a light pulse in an optical Kerr medium with balanced dispersion and self-phase modulation. This condition can be easily satisfied by dispersion engineering of a waveguide structure. SCG was demonstrated on single LNOI ridge waveguides [55,258,259] and thin-film PPLN ridge waveguides [174,259]. Ridge waveguides were dispersion-engineered for SHG and higher harmonics when pumped by femtosecond laser pulses, thereby allowing for a high spectral overlap between the SCG and SHG components. The harmonics undergo spectral broadening and merge together to form SCG when the pump power of the femtosecond laser increases. SCG with a supercontinuum spanning as large as more than 2.5 octaves from 400 nm to 2400 nm was observed on a thin-film PPLN ridge waveguide [174] [Figs. 18(a) and 18(b)]. SHG and SCG in single LNOI waveguides were used to stabilize the carrier–envelope offset frequency using self-referencing [174,258,259]. Dispersion engineering, group-velocity matching, and fabrication resolution of LNOI waveguides should be carefully performed to produce a highly efficient self-referencing with a strong f_{ceo} beatnote. This was performed in a thin-film PPLN waveguide for SCG with a spanning range of 700–2200 nm

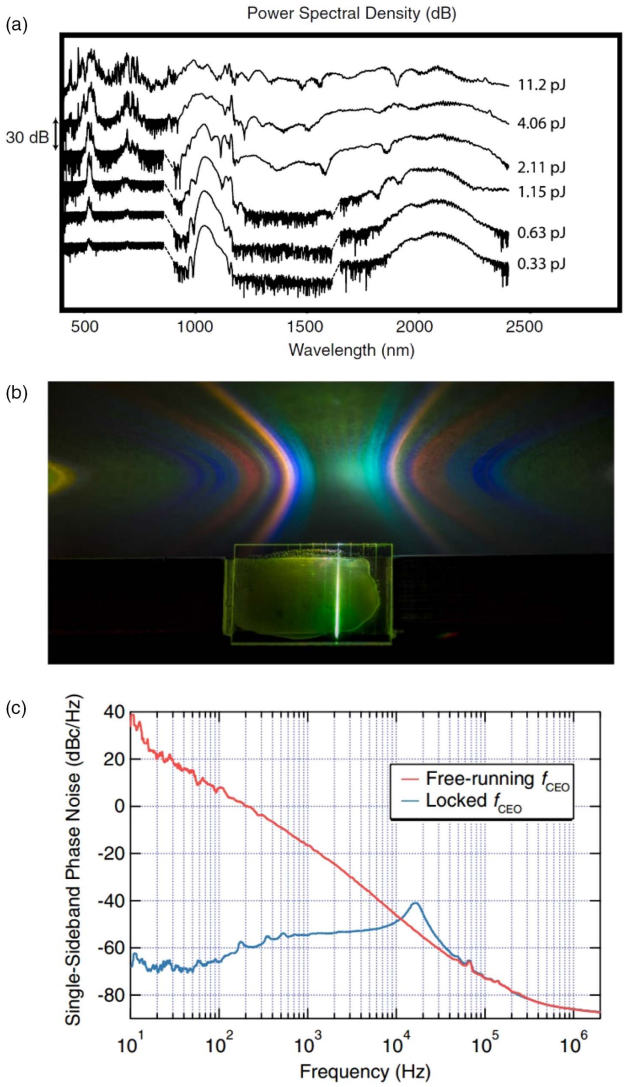

Fig. 18. (a) SCG spectra at different pump pulse energies in the thin-film PPLN waveguide. (b) Camera photo of SCG [174]. (c) Single-sideband phase noise of f_{ceo} for free-running (red) and locked conditions (blue) showing a large reduction in the phase noise (>100 dB/Hz at 10 Hz) for a locked operation [259].

using a low coupled pulse energy of 107 pJ [259]. The f_{ceo} stabilization of a mode-locked fiber laser was demonstrated with a large reduction in the phase noise >100 dB/Hz at 10 Hz [Fig. 18(c)]. SCG will enable a new capability in precision frequency metrology and frequency comb.

5. Rare Earth Ion-Doped Devices for Laser Sources

Pure LN is a passive dielectric substrate, and optical gain originates from nonlinear optical effects, such as Raman scattering and Brillouin scattering [243,244,260]. In contrast, the incorporation of a rare-earth element into the LN PIC enables active photonic applications in classical and quantum information processing [261–271]. Rare-earth elements, such as neodymium (Nd), thulium (Tm), erbium (Er), and yttrium (Yb), can be either homogeneously doped in the bulk LN during crystal growth or surface-doped to the LN by ion diffusion at temperatures typically higher than 1100°C or ion implantation [261–271]. Rare-earth-doped Ti diffused waveguides were demonstrated for waveguide lasers and laser amplifiers [266,268,271]. LNOI devices possess a small footprint and a lower loss; thus, rare-earth-doped LNOI devices allow for low-threshold lasers and high-gain amplifiers. An LN thin-film ion slicing from the pre-diffusion of the Er ion into the LN crystal by diffusion doping was successfully bonded on the silica layer on an LN substrate [269]. A thin-film Er:LN ridge waveguide was then fabricated by optical blade dicing with 1.4 dB/cm propagation loss. Consequently, fluorescence with several peaks was observed when pumping the ridge waveguide at the 980 nm and 1480 nm wavelengths [269]. Wang *et al.* implanted Er ions into the LNOI ridge waveguides and microrings with an average implantation depth of 50 nm by ion implantation [261] [Fig. 19(a)]. Post-implantation annealing was performed with a temperature higher than 350°C to repair the lattice damage from the ion implantation. The Q factor of the microring was raised to 5×10^5, which was often lower than that of the undoped microring, when the annealing temperature was 550°C. The fluorescence at the 1532 nm wavelength with a 3.2 ms lifetime, which was longer than that of doped bulk LN [Fig. 19(b)], was characterized when the microring was pumped at the 1480 nm wavelength at 1.7 K. A Tm^{3+} doped LN thin film was ion sliced from the already Tm^{3+}-doped LN. A single-mode ridge waveguide at the 794 nm wavelength was then fabricated by EBL and Ar ion milling [262] [inset, Fig. 19(c)]. When pumping the ridge waveguide at the 793.3925 nm wavelength at 3.6 K with a grating coupler having 0.1% efficiency, the photoluminescence was observed at 795 nm wavelength with a full width at half maximum of 0.69 nm and a lifetime of 157.4 μs similar to those of the Tm^{3+}-doped bulk LN [Fig. 19(c)]. A narrow spectral hole

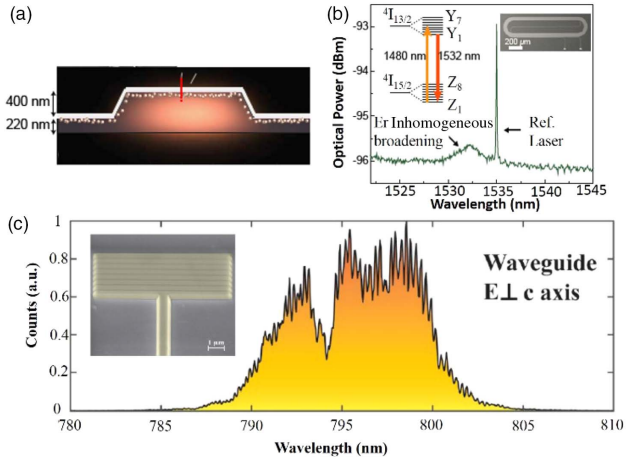

Fig. 19. Er ion-doped microring [261]: (a) schematic of the cross section of an Er ion-doped microring and fundamental TE mode; (b) non-resonant fluorescence measured at room temperature when pumping at 1480 nm, showing a small peak near 1532 nm due to the Er^{3+} fluorescence; and (c) Tm^{3+} ion-doped ridge waveguide [262] and broadband transmission spectrum filtered down to 10 nm through the waveguide with the electric field polarized perpendicular to the optical axis. Inset: SEM image of the waveguide with a grating coupler having 0.1% coupling efficiency.

at the 794 nm wavelength was demonstrated in the ridge waveguide by performing waveguide absorption measurements with the polarization of the optical electric field perpendicular to the *c* axis. The peak power for burning a hole to transparency in the ridge waveguide using a 12.5 μs long laser pulse was 10 nW, which was two orders of magnitude lower than reported in bulk waveguides. Although the photoluminescence from the rare-earth-doped thin-film LN can maintain the optical property of that from the doped bulk LN, much effort should be made to realize a low-threshold laser and a high-optical-gain amplifier by optimizing the photonic structure, coupling efficiency, and rare-earth ion-doped LNOI in the future.

C. Other PICs

In principle, the LNOI has a great potential of becoming a platform for integrated photonics for its excellent electro-optic properties and low-loss feature ranging from the visible to mid-infrared band. With the tremendous efforts made in the past, great progresses have been achieved in developing building blocks, such as waveguides, resonators, and modulators, for scalable and high-performance LNOI PICs. In this section, we will review the latest works on other building blocks ranging from couplers, delay lines, and polarizers to splitters of a prototype PIC chip.

1. Optical Interfacing

A huge mismatch in size was found between the optical mode of a standard optical fiber and that within an LNOI waveguide due to the larger refractive index contrast between the core and the claddings (e.g., air, SiO_2, Ta_2O_5) of an LNOI waveguide. The cross-sectional area of a standard single-mode optical fiber core (~9 μm) is larger than that of the LNOI waveguide (from several hundred nanometers to a few micrometers); hence, components such as grating and edge couplers are required to tackle the mode mismatch. Edge couplers generally have a relatively high coupling efficiency and work in a broadband manner, but are difficult to manipulate. On the contrary, the alignment of the input/output fiber and the grating coupler is much easier and more flexible than for the edge couplers (grating coupler can be put anywhere on a chip) at the cost of efficiency, working bandwidth, and footprint [Fig. 20(a)] [261].

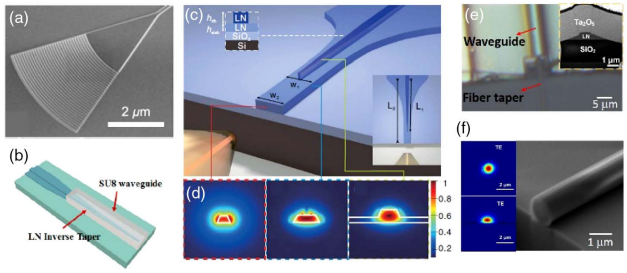

Fig. 20. (a) Grating coupler [261]. (b) LN inverse taper covered with an SU8 waveguide for the edge coupler [272]. (c) Bilayer inverse taper for the edge coupler [273] and (d) mode field conversion in space. (e) Fiber taper coupled with ridge waveguide [274]. Inset: SEM image of the cross section of the ridge waveguide. (f) SEM image of the fiber taper with 1.4 μm diameter and TE mode field distributions of the fiber taper (upper inset) and ridge waveguide (lower inset).

A fiber-to-chip grating coupler with a metal bottom reflector was experimentally demonstrated and showed a coupling efficiency of 6.9 dB for the TE mode at 1550 nm wavelength [275]. The coupling efficiencies of ~44.6%/facet and ~19.4%/facet for the TE and TM modes, respectively, were also achieved by the grating coupler [276]. Although the grating coupler [Fig. 20(a)] allowed out-of-plane coupling, it suffered from a relatively high coupled loss. An edge coupler consisting of a spot-size converter and a (lensed) fiber was experimentally reported. The coupling efficiency of 2.5 ± 0.5 dB/facet was demonstrated in a fiber-to-etched taper coupling at 1550 nm [277]. This value can be further reduced to 1.7 dB/facet and 1.5 dB/facet using a bilayer inversely tapered mode size converter [273] and LN inverse tapers covered with an SU8 waveguide [272] [Figs. 20(c) and 20(b)], respectively. Using a modal-field matched adiabatically tapered single-mode optical fiber coupling with the LNOI ridge waveguide, the coupling losses of 1.32 dB/facet and 1.88 dB/facet were experimentally reported for the TE and TM modes, respectively [274] [Figs. 20(e) and 20(f)]. If the waveguide facets are coated with an anti-reflection film, coupling losses as low as 0.32 dB/facet and 0.86 dB/facet would be achieved for the TE and TM modes, respectively, in the simulation. Much effort should be contributed to depressing the coupling loss of the LNOI waveguide, which is still higher than that of the SOI and Si_3N_4 waveguide [278] at 0.223 dB/facet [279] and 0.132 dB/facet [280], respectively.

2. Optical True Delay Line

An optical delay line consisting of a very long low-loss waveguide has attracted significant interest in rotation sensing, microwave photonics, and all-optical signal and quantum information processing [127,281]. Electro-optically switchable optical true delay lines (OTDLs) were demonstrated based on X-cut LNOI ridge waveguides by PLACE [32,182]. The largest length of a single waveguide delay line was more than 1.1 m. Figure 21 illustrates the layout of the electro-optically switchable OTDL comprising two OTDLs (i.e., OTDL I and OTDL II) of 11.22 cm and 23.06 cm lengths, respectively, and three electro-optically tunable MZIs serving as optical switches. These OTDLs provided three time delays of 0.75 ns, 1.54 ns, and 2.28 ns. Figure 21 depicts the total propagation loss of each time delay, showing the propagation loss of ~0.029 dB/cm from the slope of the fitting line in Fig. 21(c). The maximum time delay was 2.2 ns [Fig. 21(d)].

3. Wavelength/Mode (De)multiplexers

Multiplexing and demultiplexing enable the transmission of multiple light signals encoded with different wavelengths, polarizations, and modes without interference with each other from multiple fiber channels into a single fiber channel, and vice versa, to increase the capacity. The LNOI platform is an ideal platform for WDM, mode-division multiplexing (MDM), and so on due to its large electro-optic coefficients.

An arrayed waveguide grating (AWG) is an essential component in WDM communication networks. An AWG with 8×8 channels and input/output star couplers was produced by Ar ion milling [67]. The signals in the C-band wavelength range were fed into an input multiplexer (MMI, here) through eight single-mode waveguides. The signals were then diverged

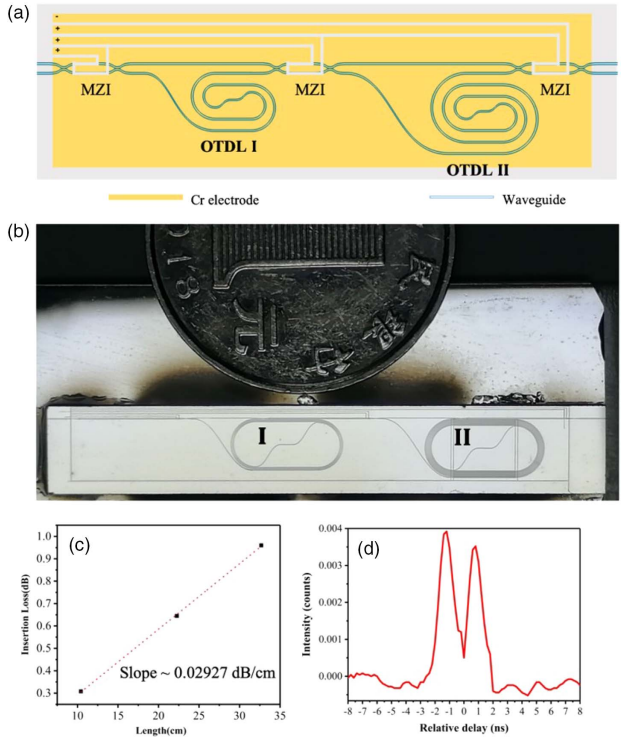

Fig. 21. Delay line based on the LNOI [32,182]. (a) Illustration of the optical true delay lines (OTDLs) layout. (b) Camera image of the two delay lines on a 3-cm-long chip. (b) Enlarged SEM image of the spiral waveguide. (c) On-chip insertion loss as a function of length of the electro-optically switchable OTDL. (d) Time delay when the signal transmits from the shortest waveguide and the two cascaded OTDLs.

into a waveguide array with 64 closely spaced single-mode waveguides at the far end. Each waveguide in the array was incrementally longer than the previous one by a constant amount; thus, the array of waveguides behaved analogously to the teeth of a blazed grating and created multiple, phase-shifted point-sources of light. These signals interfered and fed a demultiplexer (i.e., MMI), such that a dispersed spectrum was formed at the output end of the slab waveguide. The insertion loss of this MMI was 1.45 dB. The spectral response of the 8 × 500 GHz AWG in the C-band showed that the adjacent channel crosstalk was 15 dB. AWG integrated with electrodes was designed and simulated for optical filtering, thereby enabling the tuning of the central wavelength and the bandwidth [282].

Mode (de)multiplexers were also fabricated on the LNOI by an easily patterned low refractive index material (i.e., electron-beam resist ZEP520A) on an LN thin film [65] (Fig. 22). The waveguides can support the fundamental TM bound mode TM_0 and the high-order bound modes TM_1, TM_2, and TM_3 for certain waveguide widths. The high-order modes can be excited by the fundamental TM mode through multimode directional couplers with different coupling lengths. A four-channel mode (de)multiplexer at the 40 Gbit/s channel was formed by cascading the multimode directional couplers. The insertion losses for the four modes were 1.7, 3.4, 4.0, and

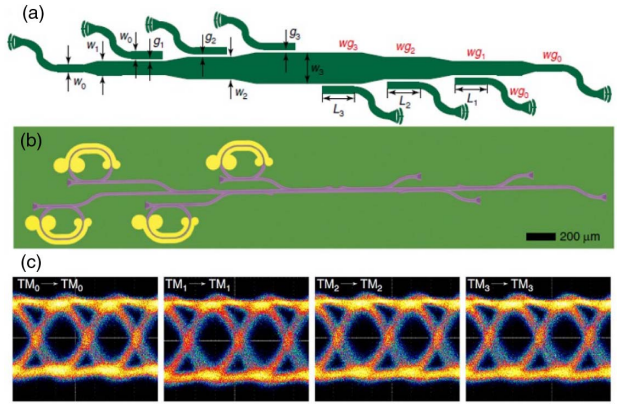

Fig. 22. Mode (de)multiplexer [65]. (a) Illustration of the (de)multiplexer, including four input ports and four output ports. (b) Fabricated device on the hybrid LNOI. (c) Four-channel TM mode (de)multiplexing at a 40 Gbit/s channel.

3.3 dB in the wavelength range of 1.51–1.58 μm. The crosstalk from the other channels to the TM_0, TM_1, TM_2, and TM_3 mode channels was −14.1, −13.8, −15.7, and −18.5 dB, respectively. The wideband response of the fabricated device showed the potential to achieve WDM and MDM simultaneously.

4. Polarization Elements

Polarization elements such as the polarizer, polarization beam splitter, polarization converter, and polarization rotator have shown great potential for integrated photonics. The designs and simulations of these devices were well reviewed by Boes *et al.* [26]. An electrical controllable TE/TM polarization converter was recently demonstrated by Chen's group using ridge waveguides on a periodically poled Z-cut LNOI [137]. A ridge waveguide oriented in the y direction with height and width of 5 μm and 6 μm, respectively, was produced by optical dicing, as schematically illustrated in Fig. 23(a). A silica buffer layer was coated, and electrodes were deposited on the sidewall of the waveguide to form transverse electrodes. An in-line polarization beam splitter was inserted before the chip to ensure that a high extinction ratio of the TE- or TM-polarized light was input. Another polarization beam splitter after the chip was used to check the output light polarization. The optical axis of different domain regions was alternately aligned at the angles of $+\theta[\approx\gamma_{51}E/(1/n_e^2 - 1/n_o^2)]$ and $-\theta$ with respect to the plane of the input light polarization [283,284] when a transverse electric field E was applied. The half-wave voltage of the polarization convertor was 13 V. The polarization was linearly polarized with all the applied voltages when the wavelength was 1590 nm, which was a quasi-phase-matched wavelength depending on the period of the PPLN. The transmission was oscillated as a varying voltage [Fig. 23(b)]. This converter exhibited a polarization extinction ratio of over 20 dB at each rotation angle. The polarization was elliptically evolved between the eigen TE and TM modes while the wavelength was 1550 nm, far from the phase matched wavelength [Fig. 23(c)].

A TM-pass polarizer was designed and simulated on hybrid plasmonic grating on the LNOI ridge waveguide with a high

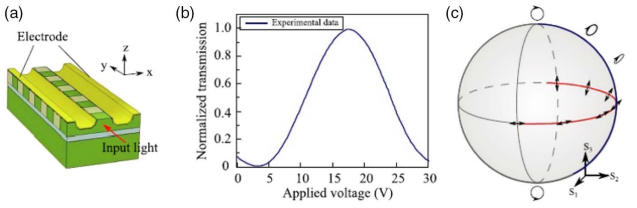

Fig. 23. (a) Schematic diagram of the ridge waveguide on the periodically poled LNOI for the electro-optically controlled TE/TM polarization. (b) Output power from the ridge waveguide after the polarizer as a function of the applied power. (c) Polarization state evolution represented on a Poincaré sphere with the applied voltage varying from 0 to 18 V when the input light wavelength is 1595 nm (red curve) or 1550 nm (blue curve) [137].

extinction ratio of 20 dB and operating at a wide waveband from 1480 nm and 1620 nm [285]. The fundamental TE and TM mode hybridization was demonstrated on an X-cut LNOI microring [186]. This hybridization showed potential for mode conversion and polarization rotation. A polarization beam splitter using an anisotropy-engineered MZI on the X-cut LNOI was more recently theoretically demonstrated, showing a high polarization extinction ratio of ~47.7 dB and a broad bandwidth of ~200 nm [286].

5. Integrated Fourier Transform Spectroscopy

An integrated high-resolution broad-spectral bandwidth spectrometer on a chip is important for precision environmental sensing. Fourier transform spectroscopy has been demonstrated on LNOI based on an electro-optically tunable closed-loop circuit [63] and an electro-optic microring dual comb [64]. A hybrid Si_3N_4–LN closed-loop circuit with gold electrodes was used to perform electro-optical tuning in Fig. 24 [63], where parallel arms with a propagation loss of 1.39 dB/cm were connected in an interference region to form a closed-loop circuit. A total of 87 discrete evanescent field samplers (EFSs) with 3 μm pitch were deposited on top of the waveguide in the interference region. The counter-propagating signals endured an opposite phase difference by applying voltage on the electrodes and led to the superposition of the standing waves. The interferogram was sampled by the EFSs by incrementally changing the applied voltage. The interferogram was electro-optically tunable; hence, the spatial sampling rate was mainly given by the voltage increment. This Fourier transform spectrometry operated with a 500 nm bandwidth ranging from 1040 nm to 1550 nm. The resolution at the 1550 nm wavelength was 5.5 nm. The electro-optic microring-based dual comb interferometer was formed by the Fourier transform of the time-domain interference pattern between two frequency combs of slightly different line spacings, revealing an RF spectrum made of the beatnotes between comb line pairs. The RF comb line spacing mapped the spectral information from the optical domain. The spectral spanning from 1.6 THz (53 cm^{-1}) at a 10 GHz resolution (0.33 cm^{-1}) was achieved [64].

6. Toward Devices of Multiple Functions

The PIC aims to integrate the whole optical system, including light sources, detectors, modulators, filters, and so on, on the

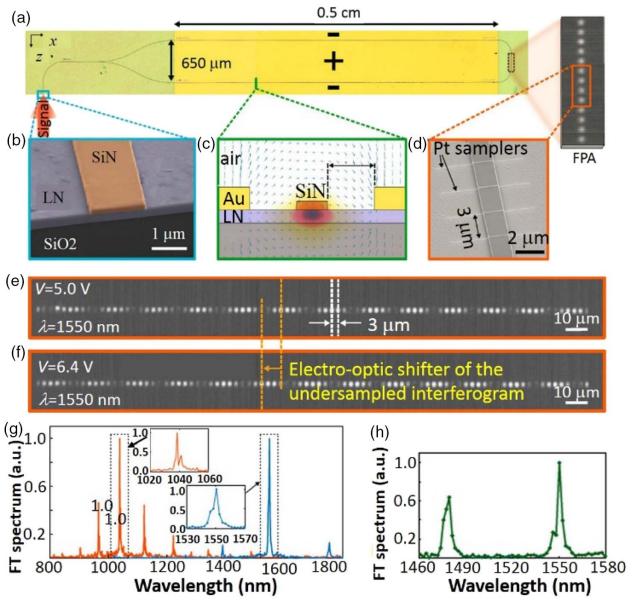

Fig. 24. Electro-optic spectrometer [63]. (a) Optical micrograph of the LN-Si_3N_4 waveguide device integrated with gold electrodes. The array of EFSs labeled in the black dashed rectangle was used to sample the intensity. (b) SEM image of the ridge waveguide. (c) Cross-sectional schematic of the waveguide–electrode configuration showing the fundamental TE mode and the applied electric field distribution (blue arrows). (d) SEM image of four platinum EFSs on top of the waveguide. (e), (f) Images of the under-sampled interferogram shift at 1550 nm with a changing voltage. (g) Reconstructed spectra for measurements at 1550 nm and 1040 nm. (h) Reconstructed Fourier transform spectrum when inputting dual wavelength of 1480 nm and 1550 nm.

same chip. The LNOI PIC is developing toward the integration of photonic devices with multiple functions [61,190,209,287]. The generation, filtering, and electro-optic modulation of the Kerr frequency comb were demonstrated on a single LNOI chip. The frequency comb [60] was generated in an X-cut LNOI microring with loaded Q of 6×10^5. The dispersion of the X-cut microring was engineered for both TM and TE modes to obtain anomalous dispersions [185]. A ridge waveguide was used to couple a continuous wave pump light into the microring to generate the frequency comb and coupled with the frequency comb into an electro-optically tunable microring with an FSR of ~1%, larger than the comb generator for filtering and modulation via the Vernier effect. The tunable microring was coupled with another ridge waveguide serving as an add–drop filter. When the 1556 nm pump power was 300 mW, the TE (TM) polarized frequency comb with a comb line spacing of ~250 GHz and a 700 nm (300 nm) spectrum range was generated. The target comb line at 1616 nm wavelength was selected by applying a DC bias voltage to drive a WGM resonant with the comb line, showing ~20 dB extinction for the comb lines adjacent to the target line. The electro-optic tuning efficiency was 2.4 pm/V. The selected comb line with 500 Mbit/s rate was demonstrated.

An electro-optically tunable coupled double-microring with 500 nm gap was fabricated for on-demand optical storage and

retrieval [204]. This strongly coupled double ring formed a photonic molecule and showed Rabi splitting with two eigenmodes separated at 14π GHz frequency. Electrodes were placed 2.5 μm away from the microring edge. The electro-optic effect in this photonic molecule was analogous to an electric dipole moment in an atomic two-level system. An external DC electric field was applied to pull the resonant frequency in opposite directions and achieve the Rabi splitting process. Microwave field with frequency matching or detuning from the energy difference of the two levels was applied to obtain second-order mode splitting or a shift in the photonic levels. They were analogous to the Autler–Townes splitting (Rabi splitting) or Stark shifts in the atomic two-level system. When a large DC voltage of 15 V was applied, the photonic molecule was reconfigured into a pair of bright and dark modes localized mainly in the first and second rings. The dark mode was accessed by applying a microwave signal with a frequency matched to the difference between the two modes. The light can be switched from the bright to dark mode by applying a microwave π pulse. The photons were trapped in the dark mode when the microwave field was turned off. After the desired storage time, the photons were retrieved back into the bright mode by applying another microwave π pulse. The dark mode lifetime was 2 ns in a microring of loaded Q of 1.9×10^6.

5. CONCLUSION AND FUTURE PERSPECTIVE

We have witnessed a revolution in the LN photonics society and industry in the past decade because of the maturity and commercialization of the LNOI material and rapid development of LNOI nanostructuring technology. The joint force has substantially changed the landscape of modern photonics because on-chip photonic microdevices now have performances close to those of bulk optics. For instance, the surface roughness of LNOI nanostructures is on the 0.1 nm level [31]; the propagation loss of LNOI waveguides is close to 0.01 dB/cm; and the Q factor of the LNOI microresonator is approaching 10^8. These performances were beyond imagination only a few years ago.

The LNOI photonic technology is evolving toward higher performance, higher integration density, and lower production cost. These demands will lead the way for technological development and industrialization of LNOI photonic devices and systems in the future. However, a series of tasks must still be accomplished before LNOI photonic technology can be widely adopted as a major PIC platform. First, device performances, including waveguide loss, Q factors of resonators, and coupling efficiencies at the optical interfaces, all need to be further improved by optimizing their design and fabrication. Second, the large-scale integration of a large amount of unit devices on one chip is unavoidable when realizing devices with a more complicated function. In this case, some fabrication techniques (e.g., EBL-assisted Ar ion milling) will be disabled by the limited fabrication area and low efficiency. The performance of the existing fabrication techniques must be improved, and new fabrication technologies aiming at high-throughput mass production should be investigated and developed. The wafer-scale integration is initially demonstrated either by deep-UV lithography-assisted Ar ion milling [192] or by PLACE [32]. However, the former process suffers from a relatively high propagation loss of the fabricated waveguides of 0.27 dB/cm, while the latter should be combined with deep-UV lithography other than laser lithography to reduce the processing time. Third, the outstanding nonlinear optical properties of LN are its features in comparison with silicon and silica. These properties should be fully brought into play. Therefore, the nonlinear optical performance of on-chip LN devices should be further optimized. This task might be tackled by fabricating high-Q PPLN resonators with carefully designed domain structures. Fourth, similar to silicon and silica, LN is difficult to make into electrically pumped light sources and detectors; thus, integrating LN devices with III–V compound semiconductor devices is worth studying for on-chip laser sources and highly efficient detectors. The 3D (vertical) integration of an LN waveguide into a silicon waveguide was already reported in a silicon–LN hybrid electro-optical modulator [71]. Although a few attempts of achieving integrated silicon and superconductor nanowire detectors have been made [288–290], the on-chip laser sources and highly efficient detectors based on the III–V compound semiconductor material hybrid integration have not yet been started. From the economic point of view, the cost of an LNOI wafer is still high compared to that of an SOI wafer and must be significantly reduced. To be compatible with today's CMOS production line, the size of an optics-grade LNOI wafer should be gradually increased from the current size of 6 inch (15.24 cm) to 8, 10, and 12 inch (20.32, 25.40, and 30.48 cm) to allow for a large-scale fabrication based on deep-UV lithography.

The development of fabrication and manufacturing technologies and the innovation of LNOI photonic devices and their widespread applications are expected to continue as the foci in the near future. The large-scale integration of PICs with on-chip laser sources, modulators, and detectors on the LNOI will pave the way for high-performance integrated quantum information processing [18,291], optical computing [292,293], telecom [48], and integrated microwave photonics [294] benefiting from the low loss of photonic devices, high-speed electro-optic modulations, high brightness $\chi^{(2)}$ nonlinear optical light sources, and excellent piezo-electric and acoustic–optical properties.

Funding. Natural Basic Research Program of China (2019YFA0705000); National Natural Science Foundation of China (11674181, 11674340, 11734009, 11822410, 11874154, 11874375, 61590934, 61761136006); Key Research Program of Frontier Sciences (QYZDJ-SSW-SLH010); Key Project of the Shanghai Science and Technology Committee (17JC1400400, 18DZ1112700); Strategic Priority Research Program of Chinese Academy of Sciences (XDB16030300); Higher Education Discipline Innovation Project (B07013); Program for Changjiang Scholars and Innovative Research Team (IRT_13R29); State Key Laboratory of Advanced Optical Communication Systems and Networks (2019GZKF03006).

Acknowledgment. We thank Min Wang, Zhiwei Fang, and Junxia Zhou from East China Normal University, Renhong

Gao from Shanghai Institute of Optics and Fine Mechanics, and Zhenzhong Hao from Nankai University for their kind help in preparation and revision of the paper.

Disclosures. The authors declare no conflicts of interest related to this paper.

REFERENCES

1. L. A. Coldren, S. W. Corzine, and M. L. Mashanovitch, *Diode Lasers and Photonic Integrated Circuits* (Wiley, 2012).
2. R. Nagarajan, C. H. Joyner, R. P. Schneider, J. S. Bostak, T. Butrie, A. G. Dentai, V. G. Dominic, P. W. Evans, M. Kato, and M. Kauffman, "Large-scale photonic integrated circuits," IEEE J. Sel. Top. Quantum Electron. **11**, 50–65 (2005).
3. V. R. Almeida, C. A. Barrios, R. R. Panepucci, and M. Lipson, "All-optical control of light on a silicon chip," Nature **431**, 1081–1084 (2004).
4. A. E.-J. Lim, J. Song, Q. Fang, C. Li, X. Tu, N. Duan, K. K. Chen, R. P.-C. Tern, and T.-Y. Liow, "Review of silicon photonics foundry efforts," IEEE J. Sel. Top. Quantum Electron. **20**, 405–416 (2014).
5. L. Pavesi, "Will silicon be the photonic material of the third millenium," J. Phys. Condens. Matter **15**, R1169–R1196 (2003).
6. J. Leuthold, C. Koos, and W. Freude, "Nonlinear silicon photonics," Nat. Photonics **4**, 535–544 (2010).
7. B. Jalali and S. Fathpour, "Silicon photonics," J. Lightwave Technol. **24**, 4600–4615 (2006).
8. W. Liu, M. Li, R. S. Guzzon, E. J. Norberg, J. S. Parker, M. Lu, L. A. Coldren, and J. Yao, "A fully reconfigurable photonic integrated signal processor," Nat. Photonics **10**, 190–195 (2016).
9. R. Nagarajan, M. Kato, D. Lambert, P. Evans, S. Corzine, V. Lal, J. Rahn, A. Nilsson, M. Fisher, M. Kuntz, J. Pleumeekers, A. Dentai, H.-S. Tsai, D. Krause, H. Sun, K.-T. Wu, M. Ziari, T. Butrie, M. Reffle, M. Mitchell, F. Kish, and D. Welch, "Terabit/s class InP photonic integrated circuits," Semicond. Sci. Technol. **27**, 094003 (2012).
10. L. Junqiu, E. Lucas, A. S. Rasa, J. He, J. Riemensberger, N. R. Wang, M. Karpov, H. Guo, R. Bouchand, and T. J. Kippenberg, "Photonic microwave generation in the X- and K-band using integrated soliton microcombs," Nat. Photonics **14**, 486–491 (2020).
11. W. D. Sacher, Y. Huang, G.-Q. Lo, and J. K. S. Poon, "Multilayer silicon nitride-on-silicon integrated photonic platforms and devices," J. Lightwave Technol. **33**, 901–910 (2015).
12. D. J. Moss, R. Morandotti, A. L. Gaeta, and M. Lipson, "New CMOS-compatible platforms based on silicon nitride and hydex for nonlinear optics," Nat. Photonics **7**, 597–607 (2013).
13. C. G. H. Roeloffzen, L. Zhuang, C. Taddei, A. Leinse, R. G. Heideman, P. W. L. van Dijk, R. M. Oldenbeuving, D. A. Marpaung, M. Burla, and K.-J. Boller, "Silicon nitride microwave photonic circuits," Opt. Express **21**, 22937–22961 (2013).
14. L. Splitthoff, M. A. Wolff, T. Grottke, and C. Schuck, "Tantalum pentoxide nanophotonic circuits for integrated quantum technology," Opt. Express **28**, 11921–11932 (2020).
15. M. Belt, M. L. Davenport, J. E. Bowers, and D. J. Blumenthal, "Ultra-low-loss Ta_2O_5-core/SiO_2-clad planar waveguides on Si substrates," Optica **4**, 532–536 (2017).
16. P. Rabiei, W. H. Steier, C. Zhang, and L. R. Dalton, "Polymer micro-ring filters and modulators," J. Lightwave Technol. **20**, 1968–1975 (2002).
17. O. Alibart, V. D'Auria, M. D. Micheli, F. Doutrev, F. Kaiser, L. Labonté, T. Lunghi, É. Picholle, and S. Tanzilli, "Quantum photonics at telecom wavelengths based on lithium niobate waveguides," J. Opt. **18**, 104001 (2016).
18. H. Jin, F. M. Liu, P. Xu, J. L. Xia, M. L. Zhong, Y. Yuan, J. W. Zhou, Y. X. Gong, W. Wang, and S. N. Zhu, "On-chip generation and manipulation of entangled photons based on reconfigurable lithium-niobate waveguide circuits," Phys. Rev. Lett. **113**, 103601 (2014).
19. Q. Li, Q. Wu, Y. Li, C. Zhang, Z. Jia, J. Yao, J. Sun, and J. Xu, "Femtosecond laser-induced periodic surface structures on lithium niobate crystal benefiting from sample heating," Photon. Res. **6**, 789–793 (2018).
20. B. Zhang, S. Li, S. Chai, X. Wu, J. Ma, L. Chen, and Y. Li, "Nonlinear distortion and spatial dispersion of intense terahertz generation in lithium niobate via the tilted pulse front technique," Photon. Res. **6**, 959–964 (2018).
21. Q. Zhang, M. Li, J. Xu, Z. Lin, H. Yu, M. Wang, Z. Fang, Y. Cheng, Q. Gong, and Y. Li, "Reconfigurable directional coupler in lithium niobate crystal fabricated by three-dimensional femtosecond laser focal field engineering," Photon. Res. **7**, 503–507 (2019).
22. F. Chen, "Photonic guiding structures in lithium niobate crystals produced by energetic ion beams," J. Appl. Phys. **106**, 081101 (2009).
23. G. Poberaj, H. Hu, W. Sohler, and P. Guenter, "Lithium niobate on insulator (LNOI) for micro-photonic devices," Laser Photon. Rev. **6**, 488–503 (2012).
24. H. Hu, J. Yang, L. Gui, and W. Sohler, "Lithium niobate-on-insulator (LNOI): status and perspectives," Proc. SPIE **8431**, 84311D (2012).
25. Y. Kong, F. Bo, W. Wang, D. Zheng, H. Liu, G. Zhang, R. Rupp, and J. Xu, "Recent progress in lithium niobate: optical damage, defect simulation, and on-chip devices," Adv. Mater. **32**, 1806452 (2020).
26. A. Boes, B. Corcoran, L. Chang, J. Bowers, and A. Mitchell, "Status and potential of lithium niobate on insulator (LNOI) for photonic integrated circuits," Laser Photon. Rev. **12**, 1700256 (2018).
27. A. Honardoost, K. Abdelsalam, and S. Fathpour, "Rejuvenating a versatile photonic material: thin-film lithium niobate," Laser Photon. Rev. **14**, 2000088 (2020).
28. M. Levy, R. M. Osgood, R. Liu, L. E. Cross, G. S. Cargill III, A. Kumar, and H. Bakhru, "Fabrication of single-crystal lithium niobate films by crystal ion slicing," Appl. Phys. Lett. **73**, 2293–2295 (1998).
29. P. Rabiei and P. Günter, "Optical and electro-optical properties of submicrometer lithium niobate slab waveguides prepared by crystal ion slicing and wafer bonding," Appl. Phys. Lett. **85**, 4603–4605 (2004).
30. A. Guarino, G. Poberaj, D. Rezzonico, R. Degl'Innocenti, and P. Günter, "Electro-optically tunable microring resonators in lithium niobate," Nat. Photonics **1**, 407–410 (2007).
31. J. Zhang, Z. Fang, J. Lin, J. Zhou, M. Wang, R. Wu, R. Gao, and Y. Cheng, "Fabrication of crystalline microresonators of high quality factors with a controllable wedge angle on lithium niobate on insulator," Nanomaterials **9**, 1218 (2019).
32. J. Zhou, R. Gao, J. Lin, M. Wang, W. Chu, W. Li, D. Yin, L. Deng, Z. Fang, J. Zhang, R. Wu, and Y. Cheng, "Electro-optically switchable optical true delay lines of meter-scale lengths fabricated on lithium niobate on insulator using photolithography assisted chemo-mechanical etching," Chin. Phys. Lett. **37**, 084201 (2020).
33. R. Wu, M. Wang, J. Xu, J. Qi, W. Chu, Z. Fang, J. Zhang, J. Zhou, L. Qiao, and Z. Chai, "Long low-loss-litium niobate on insulator waveguides with sub-nanometer surface roughness," Nanomaterials **8**, 910 (2018).
34. M. Zhang, C. Wang, R. Cheng, A. Shams-Ansari, and M. Lončar, "Monolithic ultra-high-*Q* lithium niobate microring resonator," Optica **4**, 1536–1537 (2017).
35. J. Lin, Y. Xu, Z. Fang, M. Wang, J. Song, N. Wang, L. Qiao, W. Fang, and Y. Cheng, "Fabrication of high-*Q* lithium niobate microresonators using femtosecond laser micromachining," Sci. Rep. **5**, 8072 (2015).
36. R. Wang and S. A. Bhave, "Free-standing high quality factor thin-film lithium niobate micro-photonic disk resonators," arXiv:1409.6351 (2014).
37. J. Wang, F. Bo, S. Wan, W. Li, F. Gao, J. Li, G. Zhang, and J. Xu, "High-*Q* lithium niobate microdisk resonators on a chip for efficient electro-optic modulation," Opt. Express **23**, 23072–23078 (2015).
38. C. Wang, M. J. Burek, Z. Lin, H. A. Atikian, V. Venkataraman, I.-C. Huang, P. Stark, and M. Lončar, "Integrated high quality factor lithium niobate microdisk resonators," Opt. Express **22**, 30924–30933 (2014).
39. J. Lin, Y. Xu, Z. Fang, J. Song, N. Wang, L. Qiao, W. Fang, and Y. Cheng, "Second harmonic generation in a high-*Q* lithium niobate microresonator fabricated by femtosecond laser micromachining," arXiv:1405.6473 (2014).
40. J. Lin, Y. Xu, Z. Fang, M. Wang, N. Wang, L. Qiao, W. Fang, and Y. Cheng, "Second harmonic generation in a high-*Q* lithium niobate microresonator fabricated by femtosecond laser micromachining," Sci. China Phys. Mech. Astron. **58**, 114209 (2015).

41. H. Liang, R. Luo, Y. He, H. Jiang, and Q. Lin, "High-quality lithium niobate photonic crystal nanocavities," Optica **4**, 1251–1258 (2017).
42. R. Geiss, S. Diziain, R. Iliew, C. Etrich, H. Hartung, N. Janunts, F. Schrempel, F. Lederer, T. Pertsch, and E.-B. Kley, "Light propagation in a free-standing lithium niobate photonic crystal waveguide," Appl. Phys. Lett. **97**, 131109 (2010).
43. F. Sulser, G. Poberaj, M. Koechlin, and P. Günter, "Photonic crystal structures in ion-sliced lithium niobate thin films," Opt. Express **17**, 20291–20300 (2009).
44. C. Wang, M. Zhang, X. Chen, M. Bertrand, A. Shams-Ansari, S. Chandrasekhar, P. Winzer, and M. Lončar, "Integrated lithium niobate electro-optic modulators operating at CMOS-compatible voltages," Nature **562**, 101–104 (2018).
45. M. Xu, M. He, H. Zhang, J. Jian, Y. Pan, X. Liu, L. Chen, X. Meng, H. Chen, Z. Li, X. Xiao, S. Yu, S. Yu, and X. Cai, "High-performance coherent optical modulators based on thin-film lithium niobate platform," Nat. Commun. **11**, 3911 (2020).
46. A. J. Mercante, S. Shi, P. Yao, L. Xie, R. M. Weikle, and D. W. Prather, "Thin film lithium niobate electro-optic modulator with terahertz operating bandwidth," Opt. Express **26**, 14810–14816 (2018).
47. A. J. Mercante, P. Yao, S. Shi, G. Schneider, J. Murakowski, and D. W. Prather, "110 GHz CMOS compatible thin film $LiNbO_3$ modulator on silicon," Opt. Express **24**, 15590–15595 (2016).
48. L. Shao, M. Yu, S. Maity, N. Sinclair, L. Zheng, C. Chia, A. Shams-Ansari, C. Wang, M. Zhang, K. Lai, and M. Lončar, "Microwave-to-optical conversion using lithium niobate thin-film acoustic resonators," Optica **6**, 1498–1505 (2019).
49. Y. D. Dahmani, C. J. Sarabalis, W. Jiang, F. M. Mayor, and A. H. Safavi-Naeini, "Piezoelectric transduction of a wavelength-scale mechanical waveguide," Phys. Rev. Appl. **13**, 024069 (2020).
50. W. Jiang, R. N. Patel, F. M. Mayor, T. P. McKenna, P. Arrangoiz-Arriola, C. J. Sarabalis, J. D. Witmer, R. V. Laer, and A. H. Safavi-Naeini, "Lithium niobate piezo-optomechanical crystals," Optica **6**, 845–853 (2019).
51. J. Lin, N. Yao, Z. Hao, J. Zhang, W. Mao, M. Wang, W. Chu, R. Wu, Z. Fang, and L. Qiao, "Broadband quasi-phase-matched harmonic generation in an on-chip monocrystalline lithium niobate microdisk resonator," Phys. Rev. Lett. **122**, 173903 (2019).
52. I. W. Frank, J. Moore, J. K. Douglas, R. Camacho, and M. Eichenfield, "Entangled photon generation in lithium niobate microdisk resonators through spontaneous parametric down conversion," in *Conference on Lasers and Electro-Optics (CLEO)* (IEEE, 2016), paper SM2E.6.
53. R. Luo, H. Jiang, S. Rogers, H. Liang, Y. He, and Q. Lin, "On-chip second-harmonic generation and broadband parametric down-conversion in a lithium niobate microresonator," Opt. Express **25**, 24531–24539 (2017).
54. Y. Niu, C. Lin, X. Liu, Y. Chen, X. Hu, Y. Zhang, X. Cai, Y.-X. Gong, Z. Xie, and S. Zhu, "Optimizing the efficiency of a periodically poled LNOI waveguide using in situ monitoring of the ferroelectric domains," Appl. Phys. Lett. **116**, 101104 (2020).
55. J. Lu, J. B. Surya, X. Liu, Y. Xu, and H. X. Tang, "Octave-spanning supercontinuum generation in nanoscale lithium niobate waveguides," Opt. Lett. **44**, 1492–1495 (2019).
56. A. Rao, N. Nader, M. J. Stevens, T. Gerrits, O. S. Magaña-Loaiza, G. F. Camacho-González, J. Chiles, A. Honardoost, M. Malinowski, R. Mirin, and S. Fathpour, "Photon pair generation on a silicon chip using nanophotonic periodically-poled lithium niobate waveguides," in *Conference on Lasers and Electro-Optics (CLEO)* (2018), paper JTh3C.2.
57. Z. Gong, X. Liu, Y. Xu, M. Xu, J. B. Surya, J. Lu, A. Bruch, C. Zou, and H. X. Tang, "Soliton microcomb generation at 2 μm in z-cut lithium niobate microring resonators," Opt. Lett. **44**, 3182–3185 (2019).
58. Y. He, Q.-F. Yang, J. Ling, R. Luo, H. Liang, M. Li, B. Shen, H. Wang, K. Vahala, and Q. Lin, "Self-starting bi-chromatic $LiNbO_3$ soliton microcomb," Optica **6**, 1138–1144 (2019).
59. K. Jia, X. Wang, X. Ni, J. Guo, Z. Xie, S.-W. Huang, and S.-N. Zhu, "2 μm microcomb generation from a monolithic lithium niobate optical parametric oscillator," in *Conference on Lasers and Electro-Optics (CLEO)* (2020), paper SM3L.7.
60. C. Wang, M. Zhang, M. Yu, R. Zhu, H. Hu, and M. Lončar, "Monolithic lithium niobate photonic circuits for Kerr frequency comb generation and modulation," Nat. Commun. **10**, 978 (2019).
61. M. Xu, M. He, and X. Cai, "Generation of flat optical frequency comb using integrated cascaded lithium niobate modulators," in *Conference on Lasers and Electro-Optics (CLEO)* (2020), paper STh1O.5.
62. M. Zhang, B. Buscaino, C. Wang, A. Shams-Ansari, C. Reimer, R. Zhu, J. M. Kahn, and M. Lončar, "Broadband electro-optic frequency comb generation in a lithium niobate microring resonator," Nature **568**, 373–377 (2019).
63. D. Pohl, M. R. Escalé, M. Madi, F. Kaufmann, P. Brotzer, A. Sergeyev, B. Guldimann, P. Giaccari, E. Alberti, and U. Meier, "An integrated broadband spectrometer on thin-film lithium niobate," Nat. Photonics **14**, 24–29 (2020).
64. A. Shams-Ansari, M. Yu, Z. Chen, C. Reimer, M. Zhang, N. Picque, and M. Loncar, "An integrated lithium-niobate electro-optic platform for spectrally tailored dual-comb spectroscopy," arXiv:2003.04533 (2020).
65. Z. Yu, Y. Tong, H. K. Tsang, and X. Sun, "High-dimensional communication on etchless lithium niobate platform with photonic bound states in the continuum," Nat. Commun. **11**, 2602 (2020).
66. T.-J. Wang, C.-H. Chu, and C.-Y. Lin, "Electro-optically tunable microring resonators on lithium niobate," Opt. Lett. **32**, 2777–2779 (2007).
67. M. Prost, G. Liu, and S. J. B. Yoo, "A compact thin-film lithium niobate platform with arrayed waveguide gratings and MMIs," in *Optical Fiber Communications Conference and Exposition (OFC)* (IEEE, 2018), pp. 1–3.
68. S. Fathpour, "Heterogeneous nonlinear integrated photonics," IEEE J. Quantum Electron. **54**, 6300716 (2018).
69. M. Jin, J.-Y. Chen, Y. M. Sua, and Y.-P. Huang, "High-extinction electro-optic modulation on lithium niobate thin film," Opt. Lett. **44**, 1265–1268 (2019).
70. A. Rao, A. Patil, P. Rabiei, A. Honardoost, R. DeSalvo, A. Paolella, and S. Fathpour, "High-performance and linear thin-film lithium niobate Mach-Zehnder modulators on silicon up to 50 GHz," Opt. Lett. **41**, 5700–5703 (2016).
71. M. He, M. Xu, Y. Ren, J. Jian, Z. Ruan, Y. Xu, S. Gao, S. Sun, X. Wen, and L. Zhou, "High-performance hybrid silicon and lithium niobate Mach-Zehnder modulators for 100 Gbit s^{-1} and beyond," Nat. Photonics **13**, 359–364 (2019).
72. J. Wang, W. Ji, R. Yin, Z. Gong, X. Li, S. Zhang, and C. Wu, "Integrated polarization multiplexing IQ modulator based on lithium niobate thin film and all waveguide structure," Optik **152**, 127–135 (2018).
73. M. Mahmoud, L. Cai, C. Bottenfield, and G. Piazza, "Lithium niobate electro-optic racetrack modulator etched in Y-cut LNOI platform," IEEE Photon. J. **10**, 6600410 (2018).
74. B. Zhang, L. Wang, and F. Chen, "Recent Advances in femtosecond laser processing of $LiNbO_3$ crystals for photonic applications," Laser Photon. Rev. **14**, 1900407 (2020).
75. Y. Qi and Y. Li, "Integrated lithium niobate photonics," Nanophotonics **9**, 1287–1320 (2020).
76. J. E. Toney, M. Shnider, N. Smith, P. Pontius, J. Busch, V. E. Stenger, A. Pollick, and S. Sriram, "Low voltage, high speed electro-optic scanner and switch in thin film lithium niobate," Proc. SPIE **8497**, 849709 (2012).
77. V. E. Stenger, J. E. Toney, J. Scholl, J. Busch, A. Pollick, P. Pontius, and S. Sriram, "Wide-band electro-optic modulator in thin-film lithium niobate on quartz substrate," in *38th European Conference and Exhibition on Optical Communications* (IEEE, 2012), pp. 1–3.
78. J. E. Toney, V. E. Stenger, P. Pontius, N. Smith, J. Scholl, A. Pollick, B. Sadani, H. Lu, M.-P. Bernal, and S. Sriram, "Photonic crystal electro-optic devices in engineered thin film lithium niobate substrates," Proc. SPIE **8376**, 83760H (2012).
79. K. Nassau, H. J. Levinstein, and G. M. Loiacono, "The domain structure and etching of ferroelectric lithium niobate," Appl. Phys. Lett. **6**, 228–229 (1965).
80. N. Niizeki, T. Yamada, and H. Toyoda, "Growth ridges, etched hillocks, and crystal structure of lithium niobate," Jpn. J. Appl. Phys. **6**, 318–327 (1967).

81. S. Benchabane, L. Robert, J.-Y. Rauch, A. Khelif, and V. Laude, "Highly selective electroplated nickel mask for lithium niobate dry etching," J. Appl. Phys. **105**, 094109 (2009).
82. H. J. Lee and S.-Y. Shin, "Lithium niobate ridge waveguides fabricated by wet etching," Electron. Lett. **31**, 268–269 (1995).
83. F. Laurell, J. Webjorn, G. Arvidsson, and J. Holmberg, "Wet etching of proton-exchanged lithium niobate-a novel processing technique," J. Lightwave Technol. **10**, 1606–1609 (1992).
84. V. Dobrusin, S. Ruschin, and L. Shpisman, "Fabrication method of low-loss large single mode ridge Ti: $LiNbO_3$ waveguides," Opt. Mater. **29**, 1630–1634 (2007).
85. H. Hu, R. Ricken, and W. Sohler, "Low-loss ridge waveguides on lithium niobate fabricated by local diffusion doping with titanium," Appl. Phys. B **98**, 677–679 (2010).
86. H. Hu, R. Ricken, W. Sohler, and R. B. Wehrspohn, "Lithium niobate ridge waveguides fabricated by wet etching," IEEE Photon. Technol. Lett. **19**, 417–419 (2007).
87. M. Kawabe, M. Kubota, K. Masuda, and S. Namba, "Microfabrication in $LiNbO_3$ by ion-bombardment-enhanced etching," J. Vac. Sci. Technol. **15**, 1096–1098 (1978).
88. F. Schrempel, T. Gischkat, H. Hartung, E.-B. Kley, and W. Wesch, "Ion beam enhanced etching of $LiNbO_3$," Nucl. Instrum. Methods Phys. Res. B **250**, 164–168 (2006).
89. R. Geiss, S. Saravi, A. Sergeyev, S. Diziain, F. Setzpfandt, F. Schrempel, R. Grange, E.-B. Kley, A. Tünnermann, and T. Pertsch, "Fabrication of nanoscale lithium niobate waveguides for second-harmonic generation," Opt. Lett. **40**, 2715–2718 (2015).
90. M. Minakata, "Efficient $LiNbO_3$ balanced bridge modulator/switch with an ion-etched slot," Appl. Phys. Lett. **35**, 40–42 (1979).
91. I. P. Kaminow, V. Ramaswamy, R. V. Schmidt, and E. H. Turner, "Lithium niobate ridge waveguide modulator," Appl. Phys. Lett. **24**, 622–624 (1974).
92. H. Hu, A. P. Milenin, R. B. Wehrspohn, H. Hermann, and W. Sohler, "Plasma etching of proton-exchanged lithium niobate," J. Vac. Sci. Technol. A **24**, 1012–1015 (2006).
93. J. L. Jackel, R. E. Howard, E. L. Hu, and S. P. Lyman, "Reactive ion etching of $LiNbO_3$," Appl. Phys. Lett. **38**, 907–909 (1981).
94. T. Masashi and S. Yoshikado, "Etching characteristics of $LiNbO_3$ crystal by fluorine gas plasma reactive ion etching," Sci. Technol. Adv. Mater. **2**, 563–569 (2001).
95. S. Matsui, T. Yamato, H. Aritome, and S. Namba, "Microfabrication of $LiNbO_3$ by reactive ion-beam etching," Jpn. J. Appl. Phys. **19**, L463–L465 (1980).
96. K. Noguchi, O. Mitomi, K. Kawano, and M. Yanagibashi, "Highly efficient 40 GHz bandwidth Ti:$LiNbO_3$ optical modulator employing ridge structure," IEEE Photon. Technol. Lett. **5**, 52–54 (1993).
97. W. J. Park, W. S. Yang, W. K. Kim, H. Y. Lee, J.-W. Lim, M. Isshiki, and D. H. Yoon, "Ridge structure etching of $LiNbO_3$ crystal for optical waveguide applications," Opt. Mater. **28**, 216–220 (2006).
98. P. Rabiei and W. H. Steier, "Lithium niobate ridge waveguides and modulators fabricated using smart guide," Appl. Phys. Lett. **86**, 161115 (2005).
99. Z. Ren, P. J. Heard, J. M. Marshall, P. A. Thomas, and S. Yu, "Etching characteristics of $LiNbO_3$ in reactive ion etching and inductively coupled plasma," J. Appl. Phys. **103**, 034109 (2008).
100. R. Wolf, I. Breunig, H. Zappe, and K. Buse, "Cascaded second-order optical nonlinearities in on-chip micro rings," Opt. Express **25**, 29927–29933 (2017).
101. M. Wang, R. Wu, J. Lin, J. Zhang, Z. Fang, Z. Chai, and Y. Cheng, "Chemo-mechanical polish lithography: a pathway to low loss large-scale photonic integration on lithium niobate on insulator," Quantum Eng. **1**, e9 (2019).
102. R. Wu, J. Lin, M. Wang, Z. Fang, W. Chu, J. Zhang, J. Zhou, and Y. Cheng, "Fabrication of a multifunctional photonic integrated chip on lithium niobate on insulator using femtosecond laser-assisted chemomechanical polish," Opt. Lett. **44**, 4698–4701 (2019).
103. R. Wu, J. Zhang, N. Yao, W. Fang, L. Qiao, Z. Chai, J. Lin, and Y. Cheng, "Lithium niobate micro-disk resonators of quality factors above 10^7," Opt. Lett. **43**, 4116–4119 (2018).
104. S. Diziain, R. Geiss, M. Zilk, F. Schrempel, E.-B. Kley, A. Tünnermann, and T. Pertsch, "Mode analysis of photonic crystal L3 cavities in self-suspended lithium niobate membranes," Appl. Phys. Lett. **103**, 251101 (2013).
105. S. Yin, "Fabrication of high-aspect-ratio submicron-to-nanometer range microstructures in $LiNbO_3$ for the next generation of integrated optoelectronic devices by focused ion beams (FIB)," Microw. Opt. Technol. Lett. **22**, 396–398 (1999).
106. F. Lacour, N. Courjal, M.-P. Bernal, A. Sabac, C. Bainier, and M. Spajer, "Nanostructuring lithium niobate substrates by focused ion beam milling," Opt. Mater. **27**, 1421–1425 (2005).
107. B. Gao, M. Ren, W. Wu, H. Hu, W. Cai, and J. Xu, "Lithium niobate metasurfaces," Laser Photon. Rev. **13**, 1800312 (2019).
108. V. S. Ilchenko, A. A. Savchenkov, A. B. Matsko, and L. Maleki, "Nonlinear optics and crystalline whispering gallery mode cavities," Phys. Rev. Lett. **92**, 043903 (2004).
109. M. Wang, N. Yao, R. Wu, Z. Fang, S. Lv, J. Zhang, L. Qiao, J. Lin, W. Fang, and Y. Cheng, "Strong nonlinear optics in on-chip coupled lithium niobate microdisk photonic molecules," New J. Phys. **22**, 073030 (2020).
110. L.-K. Chen and Y.-F. Xiao, "On-chip lithium niobate microresonators for photonics applications," Sci. China Phys. Mech. Astron. **63**, 224231 (2020).
111. R. Luo, Y. He, H. Liang, M. Li, and Q. Lin, "Highly tunable efficient second-harmonic generation in a lithium niobate nanophotonic waveguide," Optica **5**, 1006–1011 (2018).
112. R. Luo, Y. He, H. Liang, M. Li, J. Ling, and Q. Lin, "Optical parametric generation in a lithium niobate microring with modal phase matching," Phys. Rev. Appl. **11**, 034026 (2019).
113. J. Lu, J. B. Surya, X. Liu, A. W. Bruch, Z. Gong, Y. Xu, and H. X. Tang, "Periodically poled thin-film lithium niobate microring resonators with a second-harmonic generation efficiency of 250,000%/W," Optica **6**, 1455–1460 (2019).
114. M. Li, H. Liang, R. Luo, Y. He, J. Ling, and Q. Lin, "Photon-level tuning of photonic nanocavities," Optica **6**, 860–863 (2019).
115. C. Wang, X. Xiong, N. Andrade, V. Venkataraman, X.-F. Ren, G.-C. Guo, and M. Lončar, "Second harmonic generation in nanostructured thin-film lithium niobate waveguides," Opt. Express **25**, 6963–6973 (2017).
116. J.-Y. Chen, Z.-H. Ma, Y. M. Sua, Z. Li, C. Tang, and Y.-P. Huang, "Ultra-efficient frequency conversion in quasi-phase-matched lithium niobate microrings," Optica **6**, 1244–1245 (2019).
117. L. Cai, A. Mahmoud, M. Khan, M. Mahmoud, and T. Mukherjee, "Acousto-optical modulation of thin film lithium niobate waveguide devices," Photon. Res. **7**, 1003–1013 (2019).
118. W. S. Yang, H.-Y. Lee, W. K. Kim, and D. H. Yoon, "Asymmetry ridge structure fabrication and reactive ion etching of $LiNbO_3$," Opt. Mater. **27**, 1642–1646 (2005).
119. G. Ulliac, B. Guichardaz, J.-Y. Rauch, S. Queste, S. Benchabane, and N. Courjal, "Ultra-smooth $LiNbO_3$ micro and nano structures for photonic applications," Microelectron. Eng. **88**, 2417–2419 (2011).
120. S. W. Kwon, W. S. Yang, H. M. Lee, W. K. Kim, H.-Y. Lee, W. J. Jeong, M. K. Song, and D. H. Yoon, "The ridge waveguide fabrication with periodically poled MgO-doped lithium niobate for green laser," Appl. Surf. Sci. **254**, 1101–1104 (2007).
121. T. Tsuchiya, K. Sugano, H. Takahashi, H. Seo, Y. Pihosh, Y. Kazoe, K. Mawatari, T. Kitamori, and O. Tabata, "Dry etching and low-temperature direct bonding process of lithium niobate wafer for fabricating micro/nano channel device," in *19th International Conference on Solid-State Sensors, Actuators and Microsystems (TRANSDUCERS)* (IEEE, 2017), pp. 1245–1248.
122. L. Wang, C. Wang, J. Wang, F. Bo, M. Zhang, Q. Gong, M. Lončar, and Y.-F. Xiao, "High-Q chaotic lithium niobate microdisk cavity," Opt. Lett. **43**, 2917–2920 (2018).
123. L. Zhang, D. Zheng, W. Li, F. Bo, F. Gao, Y. Kong, G. Zhang, and J. Xu, "Microdisk resonators with lithium-niobate film on silicon substrate," Opt. Express **27**, 33662–33669 (2019).
124. D. Jun, "Fabrication methodologies for integrated photonic devices in lithium niobate," Ph.D. thesis (National University of Singapore, 2013).
125. R. Wolf, I. Breunig, H. Zappe, and K. Buse, "Scattering-loss reduction of ridge waveguides by sidewall polishing," Opt. Express **26**, 19815–19820 (2018).

126. J. Lin, J. Zhou, R. Wu, M. Wang, Z. Fang, W. Chu, J. Zhang, L. Qiao, and Y. Cheng, "High-precision propagation-loss measurement of single-mode optical waveguides on lithium niobate on insulator," Micromachines **10**, 612 (2019).
127. S. Zhu, "Meter-level optical delay line on a low-loss lithium niobate nanophotonics chip," Chin. Phys. Lett. **37**, 080102 (2020).
128. R. Takigawa, E. Higurashi, T. Kawanishi, and T. Asano, "Lithium niobate ridged waveguides with smooth vertical sidewalls fabricated by an ultra-precision cutting method," Opt. Express **22**, 27733–27738 (2014).
129. R. Takigawa, K. Kamimura, K. Asami, K. Nakamoto, T. Tomimatsu, and T. Asano, "Fabrication of a bonded LNOI waveguide structure on Si substrate using ultra-precision cutting," Jpn. J. Appl. Phys. **59**, SBBD03 (2020).
130. G. Li, Y. Chen, H. Jiang, and X. Chen, "Broadband sum-frequency generation using d_{33} in periodically poled $LiNbO_3$ thin film in the telecommunications band," Opt. Lett. **42**, 939–942 (2017).
131. B. A. Fuchs, C. Syn, and S. P. Velsko, "Diamond turning of lithium niobate for optical applications," Appl. Opt. **31**, 5788–5793 (1992).
132. T. Nishikawa, A. Ozawa, Y. Nishida, M. Asobe, F.-L. Hong, and T. W. Hänsch, "Efficient 494 mW sum-frequency generation of sodium resonance radiation at 589 nm by using a periodically poled Zn: $LiNbO_3$ ridge waveguide," Opt. Express **17**, 17792–17800 (2009).
133. J. Sun, Y. Gan, and C. Xu, "Efficient green-light generation by proton-exchanged periodically poled $MgO:LiNbO_3$ ridge waveguide," Opt. Lett. **36**, 549–551 (2011).
134. T. Ding, Y. Zheng, and X. Chen, "Integration of cascaded electro-optic and nonlinear processes on a lithium niobate on insulator chip," Opt. Lett. **44**, 1524–1527 (2019).
135. M. F. Volk, S. Suntsov, C. E. Rüter, and D. Kip, "Low loss ridge waveguides in lithium niobate thin films by optical grade diamond blade dicing," Opt. Express **24**, 1386–1391 (2016).
136. N. Courjal, F. Devaux, A. Gerthoffer, C. Guyot, F. Henrot, A. Ndao, and M.-P. Bernal, "Low-loss $LiNbO_3$ tapered-ridge waveguides made by optical-grade dicing," Opt. Express **23**, 13983–13990 (2015).
137. T. Ding, Y. Zheng, and X. Chen, "On-chip solc-type polarization control and wavelength filtering utilizing periodically poled lithium niobate on insulator ridge waveguide," J. Lightwave Technol. **37**, 1296–1300 (2019).
138. I. Hendry, L. S. Trainor, Y. Xu, S. Coen, S. G. Murdoch, H. G. L. Schwefel, and M. Erkintalo, "Experimental observation of internally pumped parametric oscillation and quadratic comb generation in a $\chi^{(2)}$ whispering-gallery-mode microresonator," Opt. Lett. **45**, 1204–1207 (2019).
139. R. Takigawa, E. Higurashi, T. Kawanishi, and T. Asano, "Demonstration of ultraprecision ductile-mode cutting for lithium niobate microring waveguides," Jpn. J. Appl. Phys. **55**, 110304 (2016).
140. N. Courjal, B. Guichardaz, G. Ulliac, J.-Y. Rauch, B. Sadani, H.-H. Lu, and M.-P. Bernal, "High aspect ratio lithium niobate ridge waveguides fabricated by optical grade dicing," J. Phys. D **44**, 305101 (2011).
141. J. U. Fürst, D. V. Strekalov, D. Elser, M. Lassen, U. L. Andersen, C. Marquardt, and G. Leuchs, "Naturally phase-matched second-harmonic generation in a whispering-gallery-mode resonator," Phys. Rev. Lett. **104**, 153901 (2010).
142. D. V. Strekalov, A. S. Kowligy, Y.-P. Huang, and P. Kumar, "Optical sum-frequency generation in a whispering-gallery-mode resonator," New J. Phys. **16**, 053025 (2014).
143. I. S. Grudinin, A. B. Matsko, A. A. Savchenkov, D. Strekalov, V. S. Ilchenko, and L. Maleki, "Ultra high *Q* crystalline microcavities," Opt. Commun. **265**, 33–38 (2006).
144. M. Förtsch, J. U. Fürst, C. Wittmann, D. Strekalov, A. Aiello, M. V. Chekhova, C. Silberhorn, G. Leuchs, and C. Marquardt, "A versatile source of single photons for quantum information processing," Nat. Commun. **4**, 1818 (2013).
145. I. Grudinin, V. Ilchenko, A. Matsko, A. Savchenkov, and L. Maleki, *Crystalline Micro-resonators: Status and Applications* (SPIE, 2006).
146. L. Chang, Y. Li, N. Volet, L. Wang, J. Peters, and J. E. Bowers, "Thin film wavelength converters for photonic integrated circuits," Optica **3**, 531–535 (2016).
147. L. Chang, M. H. Pfeiffer, N. Volet, M. Zervas, J. D. Peters, C. L. Manganelli, E. J. Stanton, Y. Li, T. J. Kippenberg, and J. E. Bowers, "Heterogeneous integration of lithium niobate and silicon nitride waveguides for wafer-scale photonic integrated circuits on silicon," Opt. Lett. **42**, 803–806 (2017).
148. A. Rao, M. Malinowski, A. Honardoost, J. R. Talukder, P. Rabiei, P. Delfyett, and S. Fathpour, "Second-harmonic generation in periodically-poled thin film lithium niobate wafer-bonded on silicon," Opt. Express **24**, 29941–29947 (2016).
149. P. Rabiei, J. Ma, S. Khan, J. Chiles, and S. Fathpour, "Heterogeneous lithium niobate photonics on silicon substrates," Opt. Express **21**, 25573–25581 (2013).
150. L. Chen, Q. Xu, M. G. Wood, and R. M. Reano, "Hybrid silicon and lithium niobate electro-optical ring modulator," Optica **1**, 112–118 (2014).
151. P. O. Weigel, M. Savanier, C. T. DeRose, A. T. Pomerene, A. L. Starbuck, A. L. Lentine, V. Stenger, and S. Mookherjea, "Lightwave circuits in lithium niobate through hybrid waveguides with silicon photonics," Sci. Rep. **6**, 22301 (2016).
152. L. Chen, J. Nagy, and R. M. Reano, "Patterned ion-sliced lithium niobate for hybrid photonic integration on silicon," Opt. Mater. Express **6**, 2460–2467 (2016).
153. J. Chiles and S. Fathpour, "Mid-infrared integrated waveguide modulators based on silicon-on-lithium-niobate photonics," Optica **1**, 350–355 (2014).
154. A. Rao, A. Patil, J. Chiles, M. Malinowski, S. Novak, K. Richardson, P. Rabiei, and S. Fathpour, "Heterogeneous microring and Mach-Zehnder modulators based on lithium niobate and chalcogenide glasses on silicon," Opt. Express **23**, 22746–22752 (2015).
155. P. Rabiei, A. Rao, J. Chiles, J. Ma, and S. Fathpour, "Low-loss and high index-contrast tantalum pentoxide microring resonators and grating couplers on silicon substrates," Opt. Lett. **39**, 5379–5382 (2014).
156. Z. Yu, X. Xi, J. Ma, H. K. Tsang, C.-L. Zou, and X. Sun, "Photonic integrated circuits with bound states in the continuum," Optica **6**, 1342–1348 (2020).
157. C. L. Zou, J. M. Cui, F. W. Sun, X. Xiong, X. B. Zou, Z. F. Han, and G. C. Guo, "Guiding light through optical bound states in the continuum for ultrahigh-*Q* microresonators," Laser Photon. Rev. **9**, 114–119 (2015).
158. J. E. Toney, *Lithium Niobate Photonics* (Artech House, 2015).
159. H. Hu, R. Ricken, and W. Sohler, "Lithium niobate photonic wires," Opt. Express **17**, 24261–24268 (2009).
160. Z. Hao, L. Zhang, A. Gao, W. Mao, X. Lyu, X. Gao, F. Bo, F. Gao, G. Zhang, and J. Xu, "Periodically poled lithium niobate whispering gallery mode microcavities on a chip," Sci. China Phys. Mech. Astron. **61**, 114211 (2018).
161. M. Chauvet, F. Henrot, F. Bassignot, F. Devaux, L. Gauthier-Manuel, V. Pêcheur, H. Maillotte, and B. Dahmani, "High efficiency frequency doubling in fully diced $LiNbO_3$ ridge waveguides on silicon," J. Opt. **18**, 085503 (2016).
162. H. Hu, L. Gui, R. Ricken, and W. Sohler, "Towards nonlinear photonic wires in lithium niobate," Proc. SPIE **7604**, 76040R (2010).
163. P. Mackwitz, M. Rüsing, G. Berth, A. Widhalm, K. Müller, and A. Zrenner, "Periodic domain inversion in x-cut single-crystal lithium niobate thin film," Appl. Phys. Lett. **108**, 152902 (2016).
164. R. V. Gainutdinov, T. R. Volk, and H. H. Zhang, "Domain formation and polarization reversal under atomic force microscopy-tip voltages in ion-sliced $LiNbO_3$ films on $SiO_2/LiNbO_3$ substrates," Appl. Phys. Lett. **107**, 162903 (2015).
165. G.-H. Shao, Y.-H. Bai, G.-X. Cui, C. Li, X.-B. Qiu, D.-Q. Geng, D. Wu, and Y.-Q. Lu, "Ferroelectric domain inversion and its stability in lithium niobate thin film on insulator with different thicknesses," AIP Adv. **6**, 075011 (2016).
166. Z. Hao, L. Zhang, W. Mao, A. Gao, X. Gao, F. Gao, F. Bo, G. Zhang, and J. Xu, "Second-harmonic generation using d_{33} in periodically poled lithium niobate microdisk resonators," Photon. Res. **8**, 311 (2020).
167. C. Wang, C. Langrock, A. Marandi, M. Jankowski, M. Zhang, B. Desiatov, M. M. Fejer, and M. Lončar, "Ultrahigh-efficiency

wavelength conversion in nanophotonic periodically poled lithium niobate waveguides," Optica **5**, 1438–1441 (2018).
168. X. Chen, P. Karpinski, V. Shvedov, K. Koynov, B. Wang, J. Trull, C. Cojocaru, W. Krolikowski, and Y. Sheng, "Ferroelectric domain engineering by focused infrared femtosecond pulses," Appl. Phys. Lett. **107**, 141102 (2015).
169. D. Feng, N. B. Ming, J. F. Hong, Y. S. Yang, J. S. Zhu, Z. Yang, and Y. N. Wang, "Enhancement of second-harmonic generation in $LiNbO_3$ crystals with periodic laminar ferroelectric domains," Appl. Phys. Lett. **37**, 607–609 (1980).
170. L. Zhang, Z. Hao, W. Mao, A. Gao, F. Bo, F. Gao, G. Zhang, and J. Xu, "Biperiodically poled lithium niobate microcavities for multiple nonlinear optical processes," in *Conference on Lasers and Electro-Optics (CLEO)* (2020), paper JTh2E.17.
171. J.-Y. Chen, Y. M. Sua, Z.-H. Ma, C. Tang, Z. Li, and Y.-P. Huang, "Efficient parametric frequency conversion in lithium niobate nanophotonic chips," OSA Contin. **2**, 2914–2924 (2019).
172. J. Zhao, C. Ma, M. Rusing, and S. Mookherjea, "High quality entangled photon pair generation in periodically poled thin-film lithium niobate waveguides," Phys. Rev. Lett. **124**, 163603 (2020).
173. J. Zhao, M. Rusing, and S. Mookherjea, "Optical diagnostic methods for monitoring the poling of thin-film lithium niobate waveguides," Opt. Express **27**, 12025–12038 (2019).
174. M. Jankowski, C. Langrock, B. Desiatov, A. Marandi, C. Wang, M. Zhang, C. R. Phillips, M. Lončar, and M. M. Fejer, "Ultrabroadband nonlinear optics in nanophotonic periodically poled lithium niobate waveguides," Optica, **7**, 40–46 (2020).
175. J. T. Nagy, K. Prabhakar, and R. M. Reano, "*In situ* temporal periodic poling of lithium niobate thin films," in *Conference on Lasers and Electro-Optics (CLEO)* (2020), paper SW3F.3.
176. J. Zhao, M. Ruesing, M. Roeper, L. M. Eng, and S. Mookherjea, "Poling thin-film x-cut lithium niobate for quasi-phase matching with sub-micrometer periodicity," J. Appl. Phys. **127**, 193104 (2020).
177. G. Ulliac, V. Calero, A. Ndao, F. Baida, and M.-P. Bernal, "Argon plasma inductively coupled plasma reactive ion etching study for smooth sidewall thin film lithium niobate waveguide application," Opt. Mater. **53**, 1–5 (2016).
178. S. Y. Siew, E. J. H. Cheung, H. Liang, A. Bettiol, N. Toyoda, B. Alshehri, E. Dogheche, and A. J. Danner, "Ultra-low loss ridge waveguides on lithium niobate via argon ion milling and gas clustered ion beam smoothening," Opt. Express **26**, 4421–4430 (2018).
179. C. Wang, M. Zhang, B. Stern, M. Lipson, and M. Lončar, "Nanophotonic lithium niobate electro-optic modulators," Opt. Express **26**, 1547–1555 (2018).
180. I. Krasnokutska, J.-L. J. Tambasco, X. Li, and A. Peruzzo, "Ultra-low loss photonic circuits in lithium niobate on insulator," Opt. Express **26**, 897–904 (2018).
181. B. Desiatov, A. Shams-Ansari, M. Zhang, C. Wang, and M. Lončar, "Ultra-low-loss integrated visible photonics using thin-film lithium niobate," Optica **6**, 380–384 (2019).
182. J. Lin, J. Zhou, R. Gao, M. Wang, R. Wu, Z. Fang, J. Zhang, and Y. Cheng, "High-precision measurement of a propagation loss of low-loss single-mode optical waveguides on lithium niobate on insulator," Proc. SPIE **11266**, 1126607 (2020).
183. S. Li, L. Cai, Y. Wang, Y. Jiang, and H. Hu, "Waveguides consisting of single-crystal lithium niobate thin film and oxidized titanium stripe," Opt. Express **23**, 24212–24219 (2015).
184. R. Wolf, Y. Jia, S. Bonaus, C. S. Werner, S. J. Herr, I. Breunig, K. Buse, and H. Zappe, "Quasi-phase-matched nonlinear optical frequency conversion in on-chip whispering galleries," Optica **5**, 872–875 (2018).
185. Y. He, H. Liang, R. Luo, M. Li, and Q. Lin, "Dispersion engineered high quality lithium niobate microring resonators," Opt. Express **26**, 16315–16322 (2018).
186. A. Pan, C. Hu, C. Zeng, and J. Xia, "Fundamental mode hybridization in a thin film lithium niobate ridge waveguide," Opt. Express **27**, 35659–35669 (2019).
187. L. Ge, H. Jiang, B. Zhu, C. Lu, Y. Chen, and X. Chen, "Quality improvement and mode evolution of high-*Q* lithium niobate micro-disk induced by 'light annealing'," Opt. Mater. Express **9**, 1632–1639 (2019).
188. H. Jiang, H. Liang, R. Luo, X. Chen, Y. Chen, and Q. Lin, "Nonlinear frequency conversion in one dimensional lithium niobate photonic crystal nanocavities," Appl. Phys. Lett. **113**, 021104 (2018).
189. I. Krasnokutska, J.-L. J. Tambasco, and A. Peruzzo, "Tunable large free spectral range microring resonators in lithium niobate on insulator," Sci. Rep. **9**, 11086 (2019).
190. M. Churaev, S. Hönl, R. N. Wang, C. Möhl, T. Liu, J. C. Skehan, J. Riemensberger, D. Caimi, J. Liu, P. Seidler, and T. J. Kippenberg, "Hybrid Si_3N_4-$LiNbO_3$ integrated platform for electro-optic conversion," in *Conference on Lasers and Electro-Optics (CLEO)* (2020), paper STh1F.3.
191. E. L. Wooten, K. M. Kissa, A. Yi-Yan, E. J. Murphy, D. A. Lafaw, P. F. Hallemeier, D. Maack, D. J. Fritz, G. J. McBrien, and D. E. Bossi, "A review of lithium niobate modulators for fiber-optic communications systems," IEEE J. Sel. Top. Quantum. Electron. **6**, 69–82 (2000).
192. K. Luke, P. Kharel, C. Reimer, L. He, M. Loncar, and M. Zhang, "Wafer-scale low-loss lithium niobate photonic integrated circuits," Opt. Express **28**, 24452–24458 (2020).
193. J. D. Witmer, J. A. Valery, P. Arrangoiz-Arriola, C. J. Sarabalis, J. T. Hill, and A. H. Safavi-Naeini, "High-*Q* photonic resonators and electro-optic coupling using silicon-on-lithium-niobate," Sci. Rep. **7**, 46313 (2017).
194. A. N. R. Ahmed, S. Shi, M. Zablocki, P. Yao, and D. W. Prather, "Tunable hybrid silicon nitride and thin-film lithium niobate electro-optic microresonator," Opt. Lett. **44**, 618–621 (2019).
195. A. N. R. Ahmed, S. Nelan, S. Shi, P. Yao, A. Mercante, and D. W. Prather, "Subvolt electro-optical modulator on thin-film lithium niobate and silicon nitride hybrid platform," Opt. Lett. **45**, 1112–1115 (2020).
196. Y. S. Lee, G.-D. Kim, W.-J. Kim, S.-S. Lee, W.-G. Lee, and W. H. Steier, "Hybrid Si-$LiNbO_3$ microring electro-optically tunable resonators for active photonic devices," Opt. Lett. **36**, 1119–1121 (2011).
197. M. Li, J. Ling, Y. He, U. A. Javid, S. Xue, and Q. Lin, "Lithium niobate photonic-crystal electro-optic modulator," Nat. Commun. **11**, 4123 (2020).
198. M. Bazzan and C. Sada, "Optical waveguides in lithium niobate: recent developments and applications," Appl. Phys. Rev. **2**, 040603 (2015).
199. M. Wang, Y. Xu, Z. Fang, Y. Liao, P. Wang, W. Chu, L. Qiao, J. Lin, W. Fang, and Y. Cheng, "On-chip electro-optic tuning of a lithium niobate microresonator with integrated in-plane microelectrodes," Opt. Express **25**, 124–129 (2017).
200. J. Holzgrafe, N. Sinclair, D. Zhu, A. Shams-Ansari, M. Colangelo, Y. Hu, M. Zhang, K. K. Berggren, and M. Loncar, "Toward efficient microwave-optical transduction using cavity electro-optics in thin-film lithium niobate," in *Conference on Lasers and Electro-Optics (CLEO)* (2020), paper FTh4D.5.
201. Y. Yang, M. Bahadori, A. E. Hassanien, L. L. Goddard, and S. Gong, "An isotropic lithium niobate microring resonator with a 1.38-nm wide continuous tuning range using 80 V," in *Conference on Lasers and Electro-Optics (CLEO)* (2020), paper JTh2F.27.
202. T.-J. Wang, G.-L. Peng, M.-Y. Chan, and C.-H. Chen, "On-chip optical microresonators with high electro-optic tuning efficiency," J. Lightwave Technol. **38**, 1851–1857 (2019).
203. M. Bahadori, L. L. Goddard, and S. Gong, "Fundamental electro-optic limitations of thin-film lithium niobate microring modulators," Opt. Express **28**, 13731–13749 (2020).
204. M. Zhang, C. Wang, Y. Hu, A. Shams-Ansari, G. Ribeill, M. Soltani, and M. Loncar, "Microwave-to-optical converter based on integrated lithium niobite coupled-resonators," in *Conference on Lasers and Electro-Optics (CLEO)* (IEEE, 2018), paper SM1I.7.
205. C. Wang, M. Zhang, X. Chen, M. Bertrand, A. Shams-Ansari, S. Chandrasekhar, P. Winzer, and M. Lončar, "100-GHz low voltage integrated lithium niobate modulators," in *Conference on Lasers and Electro-Optics (CLEO)* (IEEE, 2018), paper SM3B.4.
206. L. Chen, M. G. Wood, and R. M. Reano, "12.5 pm/V hybrid silicon and lithium niobate optical microring resonator with integrated electrodes," Opt. Express **21**, 27003–27010 (2013).

207. P. O. Weigel, J. Zhao, K. Fang, H. Al-Rubaye, D. Trotter, D. Hood, J. Mudrick, C. Dallo, A. T. Pomerene, and A. L. Starbuck, "Hybrid silicon photonic-lithium niobate electro-optic Mach–Zehnder modulator beyond 100 GHz," arXiv:1803.10365 (2018).
208. S. Jin, L. Xu, H. Zhang, and Y. Li, "$LiNbO_3$ thin-film modulators using silicon nitride surface ridge waveguides," IEEE Photon. Technol. Lett. **28**, 736–739 (2015).
209. A. S. Alam, M. Girardi, A. Caut, A. Larsson, V. Torres-Company, M. Galili, Y. Ding, and K. Yvind, "$LiNbO_3$/Si_3N_4-bilayer vertical coupler for integrated photonics," in *Conference on Lasers and Electro-Optics (CLEO)* (2020), paper STu4J.7.
210. S. Sun, M. He, S. Yu, and X. Cai, "Hybrid silicon and lithium niobate Mach-Zehnder modulators with high bandwidth operating at C-band and O-band," in *Conference on Lasers and Electro-Optics (CLEO)* (2020), paper STh1F.4.
211. A. J. Mercante, P. Yao, S. Shi, G. Schneider, J. Murakowski, and D. W. Prather, "110 GHz CMOS compatible thin film $LiNbO_3$ modulator on silicon," Opt. Express **24**, 15590–15595 (2016).
212. D. A. B. Miller, "Perfect optics with imperfect components," Optica **2**, 747–750 (2015).
213. X. Li, M. Wang, J. Li, and K. Chen, "Monolithic 1×4 reconfigurable electro-optic tunable interleaver in lithium niobate thin film," IEEE Photon. Technol. Lett. **31**, 1611–1614 (2019).
214. J. Jian, M. Xu, L. Liu, Y. Luo, J. Zhang, L. Liu, L. Zhou, H. Chen, S. Yu, and X. Cai, "High modulation efficiency lithium niobate Michelson interferometer modulator," Opt. Express **27**, 18731–18739 (2019).
215. L. Shao, W. Mao, S. Maity, N. Sinclair, Y. Hu, L. Yang, and M. Lončar, "Nonreciprocal acoustic transmission using lithium niobate parity-time-symmetric resonators," in *Conference on Lasers and Electro-Optics (CLEO)* (2020), paper FTh4Q.2.
216. L. Shao, N. Sinclair, J. Leatham, Y. Hu, M. Yu, T. Turpin, D. Crowe, and M. Loncar, "Integrated lithium niobate acousto-optic frequency shifter," in *Conference on Lasers and Electro-Optics (CLEO)* (2020), paper STh1F.5.
217. L. Shao, M. Yu, S. Maity, N. Sinclair, L. Zheng, C. Chia, A. Shams-Ansari, C. Wang, M. Zhang, K. Lai, and M. Loncar, "Integrated lithium niobate acousto-optic cavities for microwave-to-optical conversion," in *Conference on Lasers and Electro-Optics (CLEO)* (2020), paper FM2R.1.
218. Z. Yu and X. Sun, "Acousto-optic modulation of photonic bound state in the continuum," in *Conference on Lasers and Electro-Optics (CLEO)* (2020), paper STh1F.6.
219. C. J. Sarabalis, T. P. McKenna, R. N. Patel, and A. H. Safavi-Naeini, "Acousto-optics in lithium niobate-on-sapphire," in *Conference on Lasers and Electro-Optics (CLEO)* (2020), paper FTh3C.5.
220. G. Lin, A. Coillet, and Y. K. Chembo, "Nonlinear photonics with high-Q whispering-gallery-mode resonators," Adv. Opt. Photon. **9**, 828–890 (2017).
221. Y. Li, X. Jiang, G. Zhao, and L. Yang, "Whispering gallery mode microresonator for nonlinear optics," arXiv:1809.04878 (2018).
222. I. Breunig, "Three-wave mixing in whispering gallery resonators," Laser Photon. Rev. **10**, 569–587 (2016).
223. G. Lin and Y. K. Chembo, "Monolithic total internal reflection resonators for applications in photonics," Opt. Mater. X **2**, 100017 (2019).
224. M. Santandrea, M. Stefszky, and C. Silberhorn, "General framework for the analysis of imperfections in nonlinear systems," Opt. Lett. **44**, 5398–5401 (2019).
225. J. Moore, J. K. Douglas, I. W. Frank, T. A. Friedmann, R. M. Camacho, and M. Eichenfield, "Efficient second harmonic generation in lithium niobate on insulator," in *Conference on Lasers and Electro-Optics (CLEO)* (IEEE, 2016), paper STh3P.1.
226. L. Wang, L.-Q. Li, X.-T. Zhang, and F. Chen, "Type I phase matching in thin film of lithium niobate on insulator," Results Phys. **16**, 103011 (2020).
227. L. Cai, A. V. Gorbach, Y. Wang, H. Hu, and W. Ding, "Highly efficient broadband second harmonic generation mediated by mode hybridization and nonlinearity patterning in compact fiber-integrated lithium niobate nano-waveguides," Sci. Rep. **8**, 12478 (2018).
228. P. Main, P. J. Mosley, W. Ding, L. Zhang, and A. V. Gorbach, "Hybrid microfiber-lithium-niobate nanowaveguide structures as high-purity heralded single-photon sources," Phys. Rev. A **94**, 063844 (2016).
229. J. Lin, Y. Xu, J. Ni, M. Wang, Z. Fang, L. Qiao, W. Fang, and Y. Cheng, "Phase-matched second-harmonic generation in an on-chip $LiNbO_3$ microresonator," Phys. Rev. Appl. **6**, 014002 (2016).
230. H. Hu, D. Büchter, R. Ricken, and W. Sohler, "Periodically poled LNOI photonic wires," in *15th European Conference on Integrated Optics (ECIO 10)* (2010), paper FrPD3.
231. L. Gui, "Periodically poled ridge waveguides and photonic wires in $LiNbO_3$ for efficient nonlinear interactions," Ph.D. thesis (University of Paderborn, 2010).
232. L. Gui, H. Hu, M. Garcia-Granda, and W. Sohler, "Local periodic poling of ridges and ridge waveguides on X- and Y-cut $LiNbO_3$ and its application for second harmonic generation," Opt. Express **17**, 3923–3928 (2009).
233. A. Rao, K. Abdelsalam, T. Sjaardema, A. Honardoost, G. F. Camacho-Gonzalez, and S. Fathpour, "Actively-monitored periodic-poling in thin-film lithium niobate photonic waveguides with ultrahigh nonlinear conversion efficiency of 4600% W^{-1} cm^{-2}," Opt. Express **27**, 25920–25930 (2019).
234. J.-Y. Chen, Y. M. Sua, Z. Ma, L. Nguyen, and Y.-P. Huang, "Phase-sensitive amplification in nanophotonic periodically poled lithium niobate waveguides," in *Conference on Lasers and Electro-Optics (CLEO)* (2020), paper SM3L.5.
235. V. S. Ilchenko, A. B. Matsko, A. A. Savchenkov, and L. Maleki, "Low-threshold parametric nonlinear optics with quasi-phase-matched whispering-gallery modes," J. Opt. Soc. Am. B **20**, 1304–1308 (2003).
236. L. Zhang, Z. Hao, Q. Luo, A. Gao, R. Zhang, C. Yang, F. Gao, F. Bo, G. Zhang, and J. Xu, "Dual-periodically poled lithium niobate microcavities supporting multiple coupled parametric processes," Opt. Lett. **45**, 3353–3356 (2020).
237. T. Udem, R. Holzwarth, and T. W. Hänsch, "Optical frequency metrology," Nature **416**, 233–237 (2002).
238. T. J. Kippenberg, R. Holzwarth, and S. A. Diddams, "Microresonator-based optical frequency combs," Science **332**, 555–559 (2011).
239. M. Yu, C. Wang, M. Zhang, and M. Loncar, "Chip-based lithium-niobate frequency combs," IEEE Photon. Technol. Lett. **31**, 1894–1897 (2019).
240. E. Tsao and S.-W. Huang, "Monostable single dissipative Kerr soliton generation in a periodically poled lithium niobate microresonator," in *Conference on Lasers and Electro-Optics (CLEO)* (2020), paper JTu2F.27.
241. H. Jiang, R. Luo, H. Liang, X. Chen, Y. Chen, and Q. Lin, "Fast response of photorefraction in lithium niobate microresonator," Opt. Lett. **42**, 3267–3270 (2017).
242. W. Johnston, Jr., I. Kaminow, and J. Bergman, Jr., "Stimulated Raman gain coefficients for Li_6NbO_3, $Ba_2NaNb_5O_{15}$, and other materials," Appl. Phys. Lett. **13**, 190–193 (1968).
243. R. F. Schaufele and M. J. Weber, "Raman scattering by lithium niobate," Phys. Rev. **152**, 705 (1966).
244. A. B. Barker, Jr. and R. Loudon, "Dielectric properties and optical phonons in $LiNbO_3$," Phys. Rev. **158**, 433 (1967).
245. S. Spillane, T. Kippenberg, and K. Vahala, "Ultralow-threshold Raman laser using a spherical dielectric microcavity," Nature **415**, 621–623 (2002).
246. G. Lin and Y. K. Chembo, "Phase-locking transition in Raman combs generated with whispering gallery mode resonators," Opt. Lett. **41**, 3718–3721 (2016).
247. T. Hansson, D. Modotto, and S. Wabnitz, "Mid-infrared soliton and Raman frequency comb generation in silicon microrings," Opt. Lett. **39**, 6747–6750 (2014).
248. L. Maleki, A. A. Savchenkov, V. S. Ilchenko, and A. B. Matsko, "Whispering gallery mode lithium niobate microresonators for photonics applications," Proc. SPIE **5104**, 1–13 (2003).
249. M. Leidinger, B. Sturman, K. Buse, and I. J. O. I. Breunig, "Strong forward-backward asymmetry of stimulated Raman scattering in lithium-niobate-based whispering gallery resonators," Opt. Lett. **41**, 2823–2826 (2016).
250. Z. Fang, H. Luo, J. Lin, M. Wang, J. Zhang, R. Wu, J. Zhou, W. Chu, T. Lu, and Y. Cheng, "Efficient electro-optical tuning of an optical

frequency microcomb on a monolithically integrated high-*Q* lithium niobate microdisk," Opt. Lett. **44**, 5953–5956 (2019).
251. M. Yu, Y. Okawachi, R. Cheng, C. Wang, M. Zhang, A. L. Gaeta, and M. Lončar, "Raman lasing and soliton mode-locking in lithium niobate microresonators," Light Sci. Appl. **9**, e9 (2020).
252. S. Mosca, M. Parisi, I. Ricciardi, F. Leo, T. Hansson, M. Erkintalo, P. Maddaloni, P. D. Natale, S. Wabnitz, and M. D. Rosa, "Modulation instability induced frequency comb generation in a continuously pumped optical parametric oscillator," Phys. Rev. Lett. **121**, 093903 (2018).
253. A. Rueda, F. Sedlmeir, M. Kumari, G. Leuchs, and H. G. L. Schwefel, "Resonant electro-optic frequency comb," Nature **568**, 378–381 (2019).
254. C. Reimer, Y. Hu, A. Shams-Ansari, M. Zhang, and M. Lončar, "High-dimensional frequency crystals and quantum walks in electro-optic microcombs," arXiv:1909.01303 (2019).
255. T. Ren, M. Zhang, C. Wang, L. Shao, C. Reimer, Y. Zhang, O. King, R. Esman, T. Cullen, and M. Lončar, "An integrated low-voltage broadband lithium niobate phase modulator," IEEE Photon. Technol. Lett. **31**, 889–892 (2019).
256. M. Xu, M. He, X. Liu, Y. Pan, S. Yu, and X. Cai, "Integrated lithium niobate modulator and frequency comb generator based on Fabry-Perot resonators," in *Conference on Lasers and Electro-Optics (CLEO)* (2020), paper JTh2B.27.
257. B.-X. Xiang, L. Wang, Y.-J. Ma, L. Yu, H.-P. Han, and S.-C. Ruan, "Supercontinuum generation in lithium niobate ridge waveguides fabricated by proton exchange and ion beam enhanced etching," Chin. Phys. Lett. **34**, 024203 (2017).
258. M. Yu, B. Desiatov, Y. Okawachi, A. L. Gaeta, and M. Lončar, "Coherent two-octave-spanning supercontinuum generation in lithium-niobate waveguides," Opt. Lett. **44**, 1222–1225 (2019).
259. Y. Okawachi, M. Yu, B. Desiatov, B. Y. Kim, T. Hansson, M. Lončar, and A. L. Gaeta, "Chip-based self-referencing using integrated lithium niobate waveguides," Optica **7**, 702–707 (2020).
260. R. J. O'Brien, G. J. Rosasco, and A. Weber, "Brillouin scattering in lithium niobate," in *Light Scattering Spectra of Solids* (Springer, 1969), pp. 623–630.
261. S. Wang, L. Yang, R. Cheng, Y. Xu, M. Shen, R. L. Cone, C. W. Thiel, and H. X. Tang, "Incorporation of erbium ions into thin-film lithium niobate integrated photonics," arXiv:1912.07584 (2019).
262. S. Dutta, E. A. Goldschmidt, S. Barik, U. Saha, and E. Waks, "An integrated photonic platform for rare-earth ions in thin film lithium niobate," Nano Lett. **20**, 741–747 (2019).
263. C. Becker, T. Oesselke, J. Pandavenes, R. Ricken, K. Rochhausen, G. Schreiber, W. Sohler, H. Suche, R. Wessel, and S. Balsamo, "Advanced Ti:Er:$LiNbO_3$ waveguide lasers," IEEE J. Sel. Top. Quantum Electron. **6**, 101–113 (2000).
264. W. Sohler, B. K. Das, D. Dey, S. Reza, H. Suche, and R. Ricken, "Erbium-doped lithium niobate waveguide lasers," IEICE Trans. Electron. **E88-C**, 990–997 (2005).
265. Y. Sun, C. W. Thiel, and R. L. Cone, "Optical decoherence and energy level structure of 0.1% Tm^{3+}:$LiNbO_3$," Phys. Rev. B **85**, 165106 (2012).
266. X. Jiang, D. Pak, A. Nandi, Y. Xuan, and M. Hosseini, "Rare earth-implanted lithium niobate: properties and on-chip integration," Appl. Phys. Lett. **115**, 071104 (2019).
267. C. W. Thiel, T. Böttger, and R. L. Cone, "Rare-earth-doped materials for applications in quantum information storage and signal processing," J. Lumin. **131**, 353–361 (2011).
268. M. Hempstead, J. S. Wilkinson, and L. Reekie, "Waveguide lasers operating at 1084 nm in neodymium-diffused lithium niobate," IEEE Photon. Technol. Lett. **4**, 852–855 (1992).
269. C. E. Rüter, S. Suntsov, D. Kip, G. Stone, V. Dierolf, H. Hu, and W. Sohler, "Characterization of diced ridge waveguides in pure and Er-doped lithium-niobate-on-insulator (LNOI) substrates," Proc. SPIE **8982**, 89821G (2014).
270. D. Brüske, S. Suntsov, C. E. Rüter, and D. Kip, "Efficient ridge waveguide amplifiers and lasers in Er-doped lithium niobate by optical grade dicing and three-side Er and Ti in-diffusion," Opt. Express **25**, 29374–29379 (2017).
271. M. George, R. Ricken, V. Quiring, and W. Sohler, "In-band pumped Ti:Tm:$LiNbO_3$ waveguide amplifier and low threshold laser," Laser Photon. Rev. **7**, 122–131 (2013).
272. Y. Pan, S. Sun, M. Xu, M. He, S. Yu, and X. Cai, "Low fiber-to-fiber loss, large bandwidth and low drive voltage lithium niobate on insulator modulators," in *Conference on Lasers and Electro-Optics (CLEO)* (2020), paper JTh2B.10.
273. L. He, M. Zhang, A. Shams-Ansari, R. Zhu, C. Wang, and L. Marko, "Low-loss fiber-to-chip interface for lithium niobate photonic integrated circuits," Opt. Lett. **44**, 2314–2317 (2019).
274. N. Yao, J. Zhou, R. Gao, J. Lin, M. Wang, Y. Cheng, W. Fang, and L. Tong, "Efficient light coupling between an ultra-low loss lithium niobate waveguide and an adiabatically tapered single mode optical fiber," Opt. Express **28**, 12416–12423 (2020).
275. Z. Chen, Y. Wang, Y. Jiang, R. Kong, and H. Hu, "Grating coupler on single-crystal lithium niobate thin film," Opt. Mater. **72**, 136–139 (2017).
276. I. Krasnokutska, R. J. Chapman, J.-L. J. Tambasco, and A. Peruzzo, "High coupling efficiency grating couplers on lithium niobate on insulator," Opt. Express **27**, 17681–17685 (2019).
277. I. Krasnokutska, J.-L. J. Tambasco, and A. Peruzzo, "Nanostructuring of LNOI for efficient edge coupling," Opt. Express **27**, 16578–16585 (2019).
278. G. Son, S. Han, J. Park, K. Kwon, and K. Yu, "High-efficiency broadband light coupling between optical fibers and photonic integrated circuits," Nanophotonics **7**, 1845–1864 (2018).
279. S. Gröblacher, J. T. Hill, A. H. Safavi-Naeini, J. Chan, and O. Painter, "Highly efficient coupling from an optical fiber to a nanoscale silicon optomechanical cavity," Appl. Phys. Lett. **103**, 181104 (2013).
280. T. G. Tiecke, K. P. Nayak, J. D. Thompson, T. Peyronel, N. P. de Leon, V. Vuletic, and M. D. Lukin, "Efficient fiber-optical interface for nanophotonic device," Optica **2**, 70–75 (2015).
281. H. Lee, T. Chen, J. Li, O. Painter, and K. J. Vahala, "Ultra-low-loss optical delay line on a silicon chip," Nat. Commun. **3**, 867 (2012).
282. J. Li, R. Yin, W. Ji, Q. Huang, Z. Gong, L. Lv, and X. Zhou, "AWG optical filter with tunable central wavelength and bandwidth based on LNOI and electro-optic effect," Opt. Commun. **454**, 124445 (2020).
283. K. Liu, J. Shi, and X. Chen, "Linear polarization-state generator with high precision in periodically poled lithium niobate," Appl. Phys. Lett. **94**, 101106 (2009).
284. Y.-Q. Lu, Z.-L. Wan, Q. Wang, Y.-X. Xi, and N.-B. Ming, "Electro-optic effect of periodically poled optical superlattice $LiNbO_3$ and its applications," Appl. Phys. Lett. **77**, 3719–3721 (2000).
285. W. Yu, S. Dai, Q. Zhao, J. Li, and J. Liu, "Wideband and compact TM-pass polarizer based on hybrid plasmonic grating in LNOI," Opt. Express **27**, 34857–34863 (2019).
286. H. Xu, D. Dai, L. Liu, and Y. Shi, "Proposal for an ultra-broadband polarization beam splitter using an anisotropy-engineered Mach-Zehnder interferometer on the x-cut lithium-niobate-on-insulator," Opt. Express **28**, 10899–10908 (2020).
287. D. Pohl, F. Kaufmann, M. R. Escalé, J. Holzer, and R. Grange, "Tunable Bragg grating filters and resonators in lithium niobate-on-insulator waveguides," in *Conference on Lasers and Electro-Optics (CLEO)* (2020), paper STu4J.5.
288. A. A. Sayem, R. Cheng, S. Wang, and H. X. Tang, "Lithium-niobate-on-insulator waveguide-integrated superconducting nanowire single-photon detectors," Appl. Phys. Lett. **116**, 151102 (2020).
289. B. Desiatov and M. Lončar, "Silicon photodetector for integrated lithium niobate photonics," Appl. Phys. Lett. **115**, 121108 (2019).
290. M. Colangelo, B. Desiatov, D. Zhu, J. Holzgrafe, O. Medeiros, M. Lončar, and K. K. Berggren, "Superconducting nanowire single-photon detector on thin-film lithium niobate photonic waveguide," in *Conference on Lasers and Electro-Optics (CLEO)* (2020), paper SM4O.4.
291. J. Wang, F. Sciarrino, A. Laing, and M. G. Thompson, "Integrated photonic quantum technologies," Nat. Photonics **14**, 273–284 (2020).
292. Y. Shen, N. C. Harris, S. Skirlo, M. Prabhu, T. Baehr-Jones, M. Hochberg, X. Sun, S. Zhao, H. Larochelle, D. Englund, and M.

Soljačić, “Deep learning with coherent nanophotonic circuits,” Nat. Photonics **11**, 441–446 (2017).
293. Z. Ying, C. Feng, Z. Zhao, S. Dhar, H. Dalir, J. Gu, Y. Cheng, R. Soref, D. Z. Pan, and R. T. Chen, “Electronic-photonic arithmetic logic unit for high-speed computing,” Nat. Commun. **11**, 2154 (2020).
294. D. Marpaung, J. Yao, and J. Capmany, “Integrated microwave photonics,” Nat. Photonics **13**, 80–90 (2019).